Chapter 3
Molecular Dynamics Studies of Load Transfer in Nanocomposites Reinforced by Defective Carbon Nanotube

Xudong Peng and Shaker A. Meguid

Abstract This chapter is concerned with the development of relatively more accurate numerical simulations than those adopted in the literature to investigate the considerable discrepancies between experimental findings and theoretical predictions of the interfacial shear strength (ISS) of nano-reinforced thermoset composites. Those differences are most likely attributed to the presence of various defects, the possible inaccuracies in the system modeling, and the variance between experiments. In this chapter, we present a review of the literature as well as recent work conducted by the authors focusing on the effect of defects and functionalization on the ISS and buckling behavior of carbon nanotube (CNT)-reinforced composites. Different modeling and calculation techniques pertinent to CNT pull-out tests are presented, and proper selection of the simulation parameters are discussed. Unlike earlier studies, which focused on thermoplastics, in this chapter attention is devoted to CNT-reinforced thermoset polymer composites with different degrees of conversion. Pull-out and compressive load simulations were performed on a representative volume element comprising a single-walled CNT embedded in an epoxy matrix. All MD simulations used the consistent valence forcefield (CVFF) to represent the interatomic potential. Our results revealed that different defects can, to some extent, either enhance or degrade the properties of nanocomposites. The findings of this chapter will assist in improving our understanding of the toughening/weakening mechanisms associated with nanoscopic reinforcement and the load transfer capability in epoxy-based nanocomposites and give an insight into the reasons for the discrepancies in ISS.

X. Peng • S.A. Meguid (✉)

Mechanics and Aerospace Design Laboratory, Mechanical and Industrial Engineering, University of Toronto, Toronto, ON, M5S 3G8, Canada

e-mail: xpeng@mie.utoronto.ca; meguid@mie.utoronto.ca

3.1 Introduction

Since their discovery by Iijima (1991), carbon nanotubes (CNT) have attracted great interest from the mechanics and materials communities because of their promise and potential as reinforcements in polymer-based nanocomposites. These advanced polymer nanocomposites are used in various fields such as light-weight automobile and aerospace engineering, biomedical applications, energy storage devices, and molecular electronics, to name a few. The mechanical properties of CNT-reinforced composites are significantly influenced by the interface condition (cohesion and adhesion) between the CNT and the surrounding matrix. Higher interfacial shear strength (ISS) is an indicator of better stress transfer from the polymer matrix to the embedded nanotube, and hence enhanced reinforcement's effect (Desai and Haque 2005).

3.1.1 Interfacial Shear Strength

Numerous experimental efforts have been devoted to the experimental studies of the ISS of CNT-reinforced composites. Three techniques including CNT pull-out tests (depicted in Fig. 3.1), Raman spectroscopy, and fragmentation tests have been mainly used to determine the ISS experimentally. For example, Lourie and Wagner (1998, 1999) presented transmission electron microscopy (TEM)-based evidence of significant nanotube-polymer interfacial adhesion. They directly observed damage doublets and fracture of nanotubes under tensile stresses, implying strong nanotube-polymer interface. Qian and Dickey (2001) performed in-situ TEM straining studies on MWCNT-polystyrene composite films. Their experiments demonstrated significant load transfer across the nanotube-polystyrene interface by showing crack bridging, sword-in-sheath, and transverse shear fracture mechanisms. However, in a TEM study of an aligned CNT-epoxy composite, Ajayan et al. (1994) indicated the interfacial bonding between an MWCNT and epoxy matrix was weak. Schadler et al. (1998), using Raman spectroscopy, also concluded that the interfacial bonding was very weak when an MWCNT–epoxy composite was
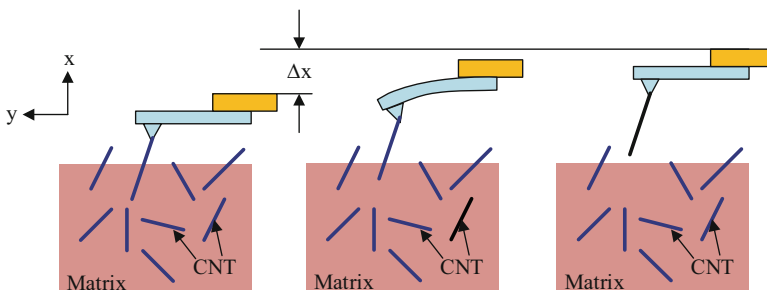

Fig. 3.1 Schematics of the procedures of CNT pull-out testing

under tension. Advances in high precision instruments at the atomic level have led to quantitative measurements of interface strength. For example, Cooper et al. (2002) calculated the ISS for single-walled CNTs (SWCNTs) and multi-walled CNTs (MWCNTs) embedded in an epoxy matrix based on pull-out experiments using a scanning probe microscope. In both cases, the ISS was found to be in the range of 35–376 MPa. Barber et al. (2003, 2004) employed an atomic force microscope (AFM) to carry out direct CNT pull-out tests. Depending on the nanotube radius, they observed an ISS of 10–130 MPa for MWCNTs embedded in the polyethylene (PE)-butene matrix. Barber et al. (2006) further investigated the effect of functionalization using both pristine and chemically modified MWCNTs in their AFM experiments. They found that for different embedded length, the measured ISS ranges from 10 to 50 MPa for pristine SWCNTs and from 20 to 165 MPa for MWCNTs. Roy et al. (2010) measured the ISS of SWCNT-polyvinyl alcohol composite functionalized with biomolecules using a novel Raman peak shift method. The ISS was found to be larger than 160 MPa. Meguid and Sun (2004) also reported that the homogeneous dispersion of CNTs in an epoxy adhesive can improve the bonding and shear properties of composite interfaces by 1.2 and 1.3 times the pure epoxy adhesive. Xu et al. (2002) added 0.1 wt% MWCNTs into thin epoxy films and observed a 20% increase in the elastic modulus using a shaft-loaded blister test. The ISS was estimated to be between 88 and 280 MPa, based on transmission electron microscopy (TEM) images. Recently, Ganesan et al. (2011, 2014) conducted in-situ pull-out experiments on pristine and fluorinated MWCNTs embedded in an epoxy matrix within an SEM using a nanoindenter assisted micro-device. The average value of ISS for the fluorinated MWCNT–epoxy interface (19.8 ± 7.78 MPa) was found to be larger than that for the pristine MWCNT–epoxy interface (6.24 ± 3.6 MPa). This demonstrated the effect of interfacial adhesion to CNT surface treatments such as sidewall fluorination. Tsuda et al. (2011) used a nano-pull-out testing system installed in an SEM to pull out MWCNTs embedded in a Poly-ether-ether-ketone (PEEK) composite. The ISS of MWCNT-PEEK composite was measured as 3.5–7 MPa, and the ISS of the specimen treated at 573 K under 1 MPa for 1 h increased to 6–14 MPa because of the recovery in interfacial bonding. Newcomb et al. (2014) characterized CNT-polyacrylonitrile (PAN) get-spun composite fibers through Raman spectroscopy by monitoring the Raman band shift during tensile deformation. The as-spun and fully drawn CNT-PAN nanocomposite fibers exhibit the ISS of 13.1 and 30.9 MPa, respectively, while improved CNT dispersion resulted in an ISS of 44.3 MPa. Chen et al. (2013) presented an in-situ nanomechanical single-tube pull-out testing scheme of the ISS between double-walled CNTs (DWCNTs) and polymethyl methacrylate (PMMA). The average ISS was reported to be within 32–68 MPa and the maximum ISS was within 85–372 MPa depending on different nanotube diameters. Chen et al. (2015) further employed the same technique to study both PMMA and epoxy materials. They found that the average ISS of the PMMA and epoxy is 45 ± 9 MPa and 130 ± 34 MPa, respectively. They further reported that the respective maximum ISS can reach 178 and 282 MPa for PMMA and epoxy considered.

Several analytical works have also been conducted to shed light on the complexities and the marked discrepancies in the reported ISS of CNT-polymer composites. A number of models such as Kelly–Tyson model, shear-lag model, and energy minimization approach previously used for the analysis of carbon fiber composites have been modified for determining the ISS of CNT-reinforced composites. For instance, Wagner et al. (1998) combined fragmentation tests with the Kelly–Tyson model modified for hollow tubes to estimate the efficiency and quality of CNT-urethane composite interfaces. The ISS obtained was to be on the order of 500 MPa and higher. Wagner (2002) further demonstrated that the ISS is dependent on the CNT strength which may be strongly reduced by the presence of defects on CNTs. Xu et al. (2002) further applied the same modified Kelly–Tyson model to theoretically calculate the ISS and found it to be in the range of 88–280 MPa for different diameters MWCNTs. Lau (2003) studied the ISS of SWCNT/MWCNT-reinforced polymer matrix through the uses of local density approximation (Lenosky et al. 1992), elastic shells (Tu and Ou-Yang 2002), and conventional fiber pull-out models (Zhou et al. 1995). The ISS increased to 200 MPa with the increase in nanotubes' wall thickness. Xiao and Zhang (2004) used a modified Cox model (Cox 1952) to investigate the effects of length and diameter of an SWCNT in an epoxy matrix on the load transfer properties. They found that the maximum ISS increases with the decrease in the CNT diameter and that there exists an optimal CNT length at which the ISS reaches its maximum. The maximum ISS was reported to be in the range of 30–100 MPa. Gao and Li (2005) modified the shear-lag model originally proposed by Cox (1952) and used a cylindrical matrix embedded with a capped SWCNT as the representative volume element (RVE) of a nano-reinforced polymer composite. The maximum ISS for different aspect ratios of the RVE was predicted to be about twice as large as the axial normal stress in the matrix. Zhang and Wang (2005) used an analytical method to investigate thermal effects on interfacial stress transfer characteristics of SWCNT/MWCNT polymer composites, based on a thermoelastic theory and conventional fiber pull-out models (Quek 2002). They found that the maximum ISS decreases from as high as 500 MPa with increasing temperature change. Furthermore, other models dedicated to CNT-reinforced composites such as multi-layer structure and structural mechanics approach have been developed to evaluate the ISS. For example, Natsuki et al. (2007) evaluated the ISS of SWCNTs/MWCNTs with composite coatings by means of a multi-layer CNT pull-out model. Their results suggested that the maximum ISS occurred at the pull-out end of CNTs and decreased from as high as 100 MPa with increasing coating thickness as well as CNT wall thickness. Li and Saigal (2007) employed a refined micromechanics model including three concentric cylinders as the RVE for assessing the ISS in CNT-reinforced polymer composites. They reported that the maximum ISS normalized by the axial normal stress in the matrix can range from 0.2 to 1.5 depending on the different volume fractions, aspect ratios, and end gaps. A multiscale model for interfacial stress transfer in SWCNT-reinforced polymer composites was developed by Li and Chou (2003a), which employed the molecular structural mechanics proposed by the same authors (Li and Chou 2003b) to characterize the nanotube and the finite element method to
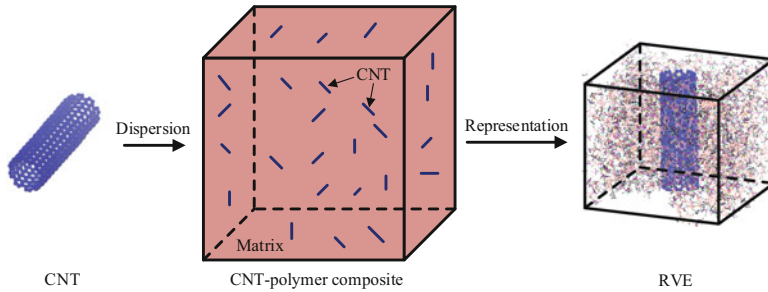
Fig. 3.2 RVE of CNT-reinforced composites

model the polymer matrix. The maximum ISS normalized by the applied stress is between 0.5 and 3 depending on the different nanotube aspect ratio and interfacial interface.

In addition to existing experimental and analytical investigations, numerous numerical simulations have also been conducted to study the interfacial behavior of CNT-reinforced composites. Molecular mechanics (MM), molecular dynamics (MD) simulations, atomistic-based continuum (ABC), and multiscale modeling technique have been mainly used to determine the ISS of an RVE (refer to Fig. 3.2) comprised of CNT-polymer composites. For instance, Wong et al. (2003) used MD simulations and elasticity calculations to quantify the ISS. They found that the non-bonded interactions, consisting of electrostatic and van der Waals forces, result in respective ISS of 138 and 186 MPa for CNT-epoxy and CNT-polystyrene systems. Gou et al. (2004, 2005) investigated the ISS of individual SWCNTs and CNT ropes via both MM and MD simulations. The ISS was calculated to be 61 and 36 MPa for an SWCNT and a three CNT rope embedded in an epoxy matrix, respectively. Wei (2006) studied the temperature dependent adhesion behavior and the reinforcement effect of CNTs in a polypropylene matrix using MD simulations. He only considered van der Waals (vdW) interactions in the model and established a lower bound ISS of approximately 47 MPa. Liao and Li (2001) used MM to simulate a pull-out process in an SWCNT-polystyrene system and reported that the ISS could be as high as 160 MPa, even without considering the chemical bonding between the nanotube and matrix. Liu et al. (2007) used MD simulations to investigate the influence of noncovalent and covalent functionalization on the interfacial properties of SWCNT-epoxy system. They found that properly designed hybrid system containing both covalent and noncovalent functionalization can increase the ISS to 940 MPa from 170 MPa for a pristine SWCNT-epoxy system. In an MD study of SWCNT-PE composite, Al-Ostaz et al. (2008) used COMPASS forcefield to obtain an ISS of 133 MPa. Li et al. (2011) further conducted pull-out simulations on SWCNT-PE systems. Instead of assuming a uniform distribution of ISS on the entire sidewalls of CNTs, they assumed that the ISS was distributed uniformly within 1 nm from each end of the CNTs but was zero at the middle of the nanotubes. The calculated ISS from this approach ranges from 106.7 to 142 MPa for different CNT diameters.

Xiong and Meguid (2015) investigated the interfacial mechanical characteristics of CNT-reinforced epoxy composites using MD simulations. They found that the ISS varies from 20 to 80 MPa as they studied various parameters, such as epoxy density, length and diameter of the CNT, the CNT-epoxy interfacial thickness, Lennard-Jones (LJ) cutoff distance, and capping conditions of a CNT. Alian et al. (2015a) used a multiscale modeling scheme to study the effect of embedded CNT length, diameter, interfacial thickness, and LJ cutoff distance. Their reported ISS values are also found to be almost identical to those predicted by Wernik et al. (2012) using ABC multiscale modeling technique.

Evidently, numerous experimental, analytical, and numerical studies have been carried out to investigate the ISS of CNT-reinforced composites. However, significant discrepancies exist among these studies. This may be partly due to the complexity of the problem and partly due to the oversimplified numerical models adopted. The simplifications included: (1) the matrix materials are usually assumed to be "frozen" during the pull-out process to avoid excessive degrees of freedom, resulting in an inappropriate estimation of the interfacial thickness and the CNT–matrix interaction energy, (2) the neglect of experimentally observed defects in CNTs, such as vacancies (Meyer et al. 2008), Stone–Wales (SW) (Suenaga et al. 2007), and interstitial atoms (Hashimoto et al. 2004), as depicted in Fig. 3.3, which
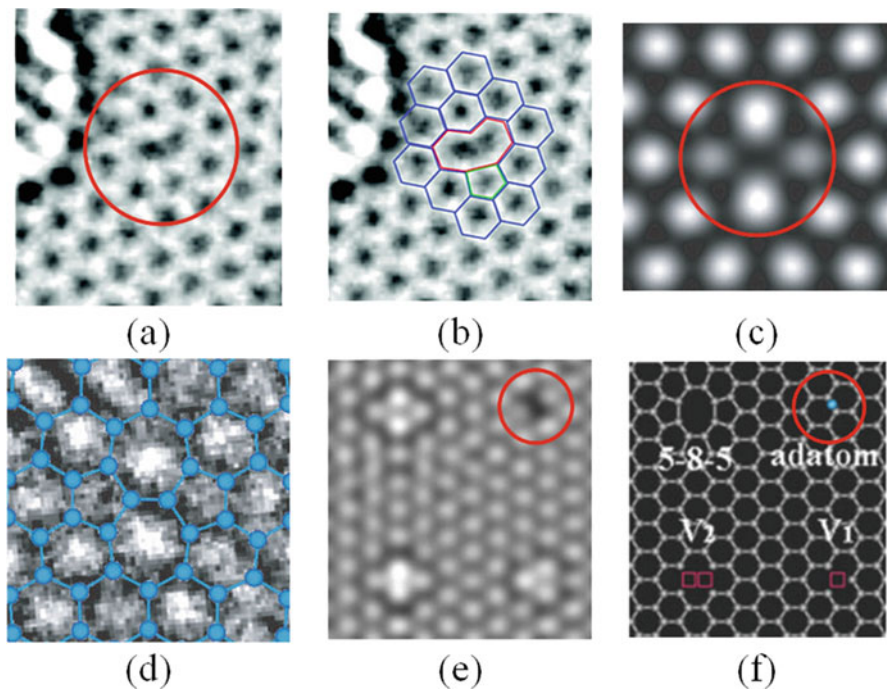
Fig. 3.3 Intrinsic defects of CNTs: (**a**, **b**) HR-TEM image of single vacancy (Meyer et al. 2008), (**c**, **d**) HR-TEM image of SW defect (Suenaga et al. 2007), (**e**, **f**) HR-TEM image of a single adatom defect (Hashimoto et al. 2004)

are inevitably introduced during CNT synthesis as well as manufacturing (Collins 2010; Charlier 2002; Nardelli et al. 1998), and (3) the neglect of covalent bonding between CNTs and matrix materials. Covalent bonding is usually introduced through surface functionalizations of CNTs (Liu et al. 2005; Spitalsky et al. 2010; Thostenson et al. 2005), which are used to improve the load transferability of nanocomposites.

In addition to the above limitations, most existing numerical models focused their attention on thermoplastic polymers (Chowdhury et al. 2010; Frankland et al. 2002; Xiao et al. 2015; Zheng et al. 2009). Numerical models which can better characterize the interfacial properties of CNT-reinforced thermoset composites systems are scarce. Thermoset materials generally have very different mechanical properties than thermoplastic materials because they comprise three-dimensional networks of bonds (crosslinking). However, to the best of authors' knowledge, there have been no studies performed on the effect of crosslink density on the interfacial properties of CNT-reinforced thermoset composites. The importance of nano-reinforced epoxy composites to many engineering applications as well as the lack of coverage in the literature has motivated the current chapter.

3.1.2   Buckling Behavior

As mentioned in Sect. 3.1.1, considerable experimental and theoretical studies have been carried out to characterize the ISS of CNT-reinforced nanocomposites. However, significant discrepancies exist between experimental and theoretical results. These theoretically obtained values are remarkably different from the experimental data. Apart from the reasons mentioned in Sect. 3.1.1, some researchers attributed the discrepancy of the results to buckled CNTs in nanocomposites.

In particular, the diameters of CNTs are in the range of less than a nanometer for SWCNTs to about 30 nm for MWCNTs while the typical length of CNTs is on the order of microns (Pan et al. 1999; Qian et al. 2000), leading to a large aspect ratio (length to diameter). Because of this large aspect ratio and hollow cylindrical structure, CNTs are prone to buckle under mechanical loads. Buckling can lead to failure in the form of a sudden decline in compressive load carrying capacity and undesirably distorted configuration of structures. Under axial compression, a CNT exhibits shell-like or beam-like buckling depending on its aspect ratio; shell-like buckling appears when the aspect ratio is relatively small, while beam-like buckling appears when the aspect ratio is relatively large. Numerous experimental and theoretical studies have investigated the buckling of CNT-reinforced nanocomposites. Experimental researchers have observed graphs of CNTs in buckled state both as individual nanotubes (Dai et al. 1996; Iijima et al. 1996; Wong et al. 1997) and when embedded in nanocomposites (Schadler et al. 1998; Lourie et al. 1998). A large volume of theoretical work, based on both

continuum-based shell and beam theories (Yakobson et al. 1996; Ru 2000; Wang et al. 2003), and atomistic techniques such as MD (Zhang et al. 2009a; Talukdar et al. 2011; Motevalli et al. 2013; Wang et al. 2014), concentrates on buckling of nanotubes by themselves. However, an increasing number of researchers are interested in the compressive behavior of nanotubes when embedded in composites. For instance, Lourie et al. (1998) coupled the classical Euler model with energy method to examine a CNT buckling behavior within a polymeric matrix. To account for the effect of transverse shear deformation during the CNT buckling, Zhang et al. (2006a) developed Timoshenko beam model, which offers a more precise prediction of the critical buckling stress. Ru (2001) developed an elastic double-walled shell model for the buckling analysis of CNTs in an elastic matrix based on the classical shell theory (Timoshenko 1961). Later, Liew et al. (2005) and Kitipornchai et al. (2005) introduced a Pasternak foundation into Ru's model (Ru 2001). They proposed multi-walled shell model to describe the buckling behavior of MWCNTs that are embedded in a matrix with consideration of the van der Waals (vdW) interactions.

Since CNTs are highly prone to structural defects and buckling, many investigations have focused on buckling of defective CNTs. For example, the MD simulations were employed by Chandra and Namilae (2006) to explore the compressive behavior of SWCNTs in the presence of chemical functionalization and SW defects. They found that functionalization and topological defects have a negative impact on the buckling stress of CNTs. The compressive behavior of SWCNTs and double-walled CNTs in the presence of vacancy defects was examined by Hao et al. (2008) and Xin et al. (2007) using MD simulations. They found that the extent to which vacancy defects weaken the compressive load carrying capacity of CNTs is dependent on the length, chirality, and temperature of the nanotubes as well as the density of the defects and their relative position. Zhang et al. (2009b) conducted an investigation into the buckling behavior of SWCNTs with defects via MD simulations. They revealed that point defects cause a higher reduction in the buckling load than SW defects. Kulathunga et al. (2010) examined the effects of various configurations of vacancy defects on the buckling of SWCNTs by MD simulations in different thermal environments. Their findings revealed that increasing number of missing atoms, asymmetry of vacancy configurations, and asymmetric distribution of vacancy clusters lead to higher deterioration in buckling properties. Ranjbartoreh and Wang (2011) studied the effects of length, radius, chirality, SW defect, and single vacancy defect on the buckling behavior of SWCNTs. Obtained results indicated that the axial stability of SWCNTs decreases significantly due to topological defects and the critical buckling strain was more susceptible to defects than the critical buckling force. Different aspect ratio of defective CNTs on the buckling behavior was investigated by Parvaneh et al. (2009), who showed that single vacancy defects only have a weak impact on the critical buckling load of CNTs with a large aspect ratio at room temperature. Poelma et al. (2012) combined analytical continuum theory with MD to study the effects of vacancy defect position on the CNT critical buckling

load. They concluded that the defects at the ends of the CNT and close to the middle of the CNT significantly reduce the critical buckling load and strain at 1 K. The compressive mechanical properties of SWCNTs with up to 20 randomly distributed vacancies were studied by Cheng et al. (2007) using MD method. It was found that the Young's modulus of the SWCNTs is approximately linearly proportional to the number of vacancies and SWCNTs containing more vacancies have more complicated deformation procedures.

It is evident from the foregoing literature review that there has been no work on the effect of various defects on the buckling of embedded CNTs. To the authors' knowledge, only a few studies have used MD simulations to focus on the buckling of embedded pristine CNTs. For instance, Namilae and Chandra (2006) studied the compressive behavior of CNTs when they are embedded in PE matrix and with interface chemical modifications using MD simulations. It is observed that the buckling load for buckling increases only very marginally for nanotubes embedded in PE matrix compared with neat CNTs. In the case of chemically bonded interfaces, the critical stress for buckling is reduced compared with neat CNTs because of the changes in curvature introduced by chemical bonding. The buckling of SWCNTs embedded in PE matrix was examined by Kulathunga and Ang (2014) via MD method. They found that the embedded CNT has higher buckling stress compared to the freestanding CNT. This stress increment is greater in CNTs with smaller aspect ratio. It is clear that there is an urgent need to carry out a comprehensive research on the buckling of defective CNTs embedded in polymer nanocomposites.

3.1.3 Objectives

It is therefore the objectives of this chapter to:

(1) Provide a critical review of different modeling techniques, CNT pull-out methods, ISS distribution models and discuss recent developments in the field.
(2) Evaluate the ISS of CNT-reinforced thermoset composites and examine the effect of the following parameters on the strength of the interface:

 (a) Defects in embedded CNTs
 (b) Presence of foreign atoms
 (c) Interfacial non-bonded (van der Waals) and bonded (covalent bonding) interactions
 (d) Buckling of embedded CNTs

(3) Investigate which of these parameters either singly or jointly have major effect on the ISS of CNT-reinforced composites.

3.2 Fundamental Aspects of MD Simulation Techniques

3.2.1 Numerical Simulation Techniques

CNT pull-out test has been recognized as a standard method for evaluating the ISS of nanocomposites. The force or energy required to debond the CNTs from the surrounding matrix is the output of these tests which are then used to calculate the ISS. The analysis of the ISS of nanocomposites is experimentally conducted using improvised scanning probe microscope (Cooper et al. 2002) and AFM (Barber et al. 2003, 2006), which require high precision instruments to measure the pull-out force because the pull-out forces are usually on the order of nanonewton. These experiments also require high-resolution microscopes such as scanning electron microscope (Barber et al. 2003, 2006) and TEM (Cooper et al. 2002) for imaging the CNTs. The challenge in experiments is manifested from the fact that relatively few experimental works have been published in the literature due to the difficulties of setting up nanoscale experiments and the inability to produce reliable high precision measuring instruments at the atomic scale. Therefore, researchers rely on atomistic-based or continuum-based methods for the ISS analysis of nanocomposites. However, continuum-based approaches such as shear-lag model (Gao and Li 2005) and Kelly–Tyson approach (Xu et al. 2002; Wagner et al. 1998) are less accurate since they do not account for the nanoscopic effects explicitly. It is also difficult to apply continuum methods to CNTs with defects and functional groups. Hence, many researchers resort to atomistic methods such as ABC, MM, and MD simulations to investigate the influence of defects and functionalization on the ISS of nanocomposites.

ABC technique is developed to model CNTs and CNT-reinforced composites by replacing the atomistic structures with equivalent continuum elements. In this technique, in contrast to traditional continuum modeling methods, the discrete nature of the structures on the atomic scale is considered by replacing bonded and non-bonded interactions with continuum elements such as beam, truss, and spring. For example, as illustrated in Fig. 3.4, Wernik and Meguid (2010) used FEA to model CNTs as space frame structures in which beam elements were successfully used to simulate carbon–carbon covalent bond, while nonlinear rotational spring element was used to model non-bonded interactions.

Fig. 3.4 Atomistic-based continuum representations of (**a**) a hexagonal lattice of the CNT, and (**b**) the connecting structural finite elements used to model the CNT

(a)   (b)
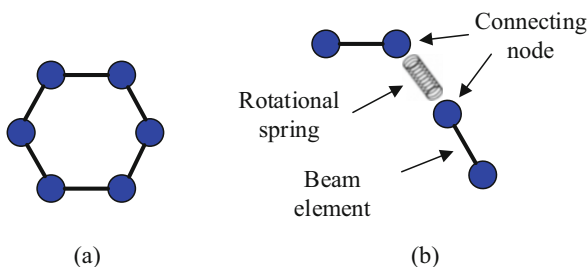
In MD and MM techniques, the atomic structures of nanocomposites are initially defined. Interactions of atoms in nanocomposites are defined by interatomic potential energy function, which is either obtained from first-principle calculations (Sun 1998), or from experimental results, such as bond energy and atomization energy (Brenner et al. 2002). In general, the interatomic potential energy is a function of the positions of atoms in nanocomposites. Force on each atom is derived from the gradient of the total potential energy in nanocomposites.

In MM, thermodynamic equilibrium is achieved by minimizing the total potential energy of the system by considering the atomic coordinates. The governing equation for MM is given by

$$\frac{\partial U(r)}{\partial r} = 0 \tag{3.1}$$

where U is the total potential energy of the system and r is the position vector of an atom.

MM does not consider time-dependent quantities like velocity, acceleration, and inertia force. Unlike MM, MD is performed by solving Newton's equation of motion for each atom in the system. The governing equations for MD are

$$m_i \frac{d^2 r_i}{dt^2} = F_i \tag{3.2}$$

and

$$F_i = -\frac{\partial U(r_1, r_2, \ldots, r_i, \ldots, r_N)}{\partial r_i} \tag{3.3}$$

where r_i is the position vector of atom i, N is the total number of atoms, and F_i is the force vector acting on atom i, m_i is the mass of ith atom, and t is the time. Since MM does not consider transient and dynamic quantities, it cannot account for the thermal effect during the CNT pull-out process. In order to determine the ISS accurately under realistic temperature, MD approach is used by the authors in this chapter.

The current MD simulations were carried out using the large-scale atomic/molecular massively parallel simulator (LAMMPS) (Plimpton 1995). The CVFF (Dauber-Osguthorpe et al. 1988) was adopted in the simulations to model all bonded and non-bonded interactions in the CNT-epoxy systems. This forcefield has been widely used by other researchers to study the mechanical properties of CNT-reinforced epoxy composites (Alian et al. 2015a, 2015b; Kumar et al. 2014; Li et al. 2012). The analytic forms (U_{pot}) of the energy expressions utilized in the CVFF are given below:

$$U_{pot} = U_{bond} + U_{angle} + U_{dihedral} + U_{improper} + U_{vdW} + U_{Coulomb} \tag{3.4}$$
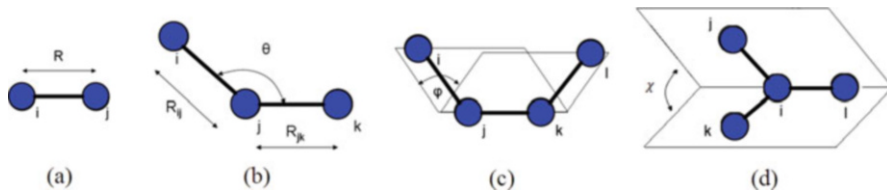
Fig. 3.5 Schematics of the different bonded CVFF terms: (**a**) bond length, (**b**) bond angle, (**c**) torsion angle, (**d**) inversion angle

where U_{bond}, U_{angle}, $U_{dihedral}$, $U_{improper}$ are the bonded interactions which represent the respective energy of deformation of bond lengths, bond angles, torsion angles, and inversion angles, U_{vdW} and $U_{Coulomb}$ are the non-bonded interactions which represent the respective van der Waals (vdW) and electrostatic interactions. The components of the potential energy due to the bonded interactions are shown in Fig. 3.5.

### 3.2.2 Molecular Modeling of Pull-Out Simulation

3.2.2.1 Molecular Structure of CNTs with Defects and Functionalization

The molecular structures of five different types of possible defects and one type of CNT functionalization considered are presented in Fig. 3.6. All defects are assumed to form onto the sidewall of an armchair (9, 9) SWCNT. As can be seen in Fig. 3.6a–c, monovacancy, bivacancy, and trivacancy were formed by removing one-, two-, and three-bonded carbon atoms from the pristine SWCNT, respectively. A single adatom presented in Fig. 3.6d is an interstitial defect formed by an extra carbon that is covalently bonded to two adjacent carbon atoms. The SW defect shown in Fig. 3.6e is formed via a 90° rotation of the carbon–carbon bond, transforming four hexagons into two pentagons and heptagons (5-7-7-5). Finally, Fig. 3.6f shows the phenyl functional group ($-C_6H_5$) which is end-grafted to the sidewall of the CNT. The phenyl group contains a benzene ring, which typically exists in epoxy resins. The associated change in geometry of the atoms is that the phenyl group becomes perpendicular to the sidewalls of CNTs and the hybridization of the bonded atom is changed from sp^2 to sp^3.

Five different defects in CNTs and one case of functionalization were considered in our research; as follows: (1) CNTs with 3, 6, 9, 12, 15, 18 monovacancies; (2) CNTs with 2, 3, 4, 5, 6, 7, 8, 9 bivacancies; (3) CNTs with 1, 2, 3, 4, 5, 6 trivacancies; (4) CNTs with 4, 8, 12 adatoms; (5) CNTs with 5, 10, 15 SW defects; and (6) Functionalized CNTs using 3, 6, 9 phenyl functional groups. The positions of the defects and functionalization were randomly located on the sidewalls of the CNTs. The simulation for each case was repeated three times, and the ISS results were averaged and curve fitted.
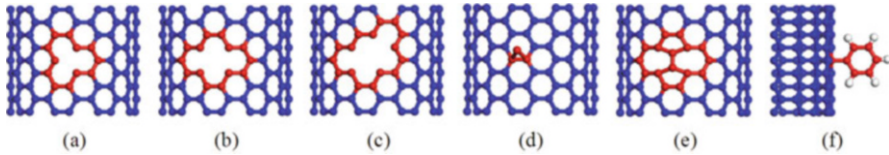
Fig. 3.6 Geometries of CNTs containing different defects and functionalization: (**a**) monovacancy, (**b**) bivacancy, (**c**) trivacancy, (**d**) single carbon adatom defect, (**e**) SW defect, and (**f**) phenyl group functionalization
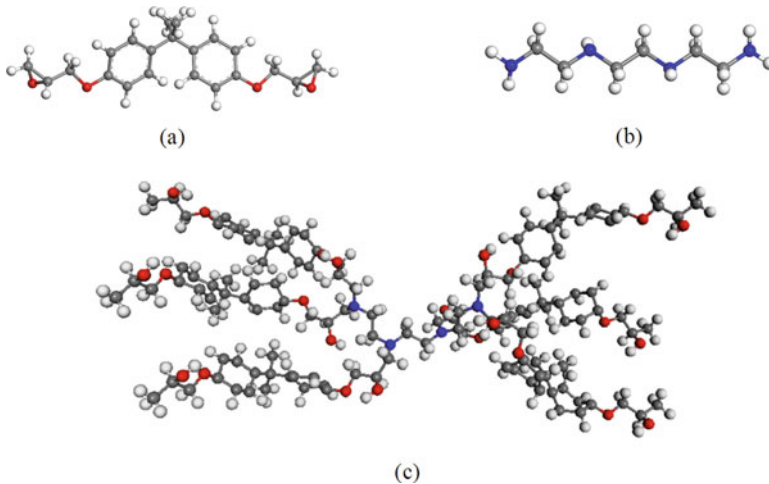
Fig. 3.7 Chemical structures of (**a**) epoxy resin (DGEBA), (**b**) curing agent (TETA), and (**c**) cured epoxy oligomer (6 DGEBA molecules connected by 1 TETA). (The hydrogen, carbon, oxygen, and nitrogen atoms of the epoxy chain are presented by white, gray, red, and blue colors, respectively)

3.2.2.2 Cured versus Uncured Polymer

The polymer used was a specific two-component epoxy resin based on a diglycidyl ether of bisphenol A (DGEBA) epoxy and triethylene tetramine (TETA) curing agent, which is typically used in the aerospace industry. Different degrees of conversion were introduced by analyzing both uncured and cured epoxy composites. Cured epoxy system was developed during the curing process by forming covalent bonds between the hydrogen atoms in the amine groups of the curing agent and the epoxide groups of the epoxy. As shown in Fig. 3.7, each epoxy oligomer consists of six DGEBA molecules connected by one TETA molecule so that the resin-hardener weight ratio in the epoxy polymer is equal to 100:16.7. Finally, 33 epoxy oligomers were packed into the RVE using Packmol software (Martínez et al. 2009) to obtain an appropriate density, and the final structure of the RVE is visualized by VMD (Humphrey et al. 1996) as shown in Fig. 3.8a. For the uncured epoxy matrix, the
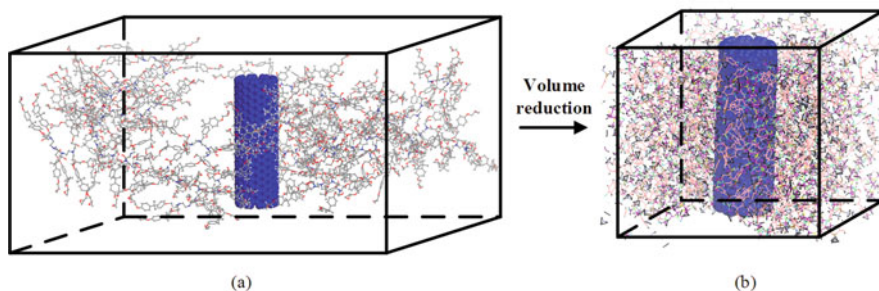
Fig. 3.8 Preparation of the RVE (**a**) SWCNT embedded in 33 randomly placed cured epoxy oligomers in a simulation box of size $150 \times 150 \times 45$ Å, and (**b**) the compressed SWCNT-epoxy system in a simulation box of size $50 \times 50 \times 42$ Å

same numbers of individual DGEBA and TETA as the cured system were used to generate the RVE. The uncured state means that there is no curing process in the epoxy matrix and no covalent bonds were formed between the DGEBA and TETA.

3.2.2.3   Construction of Nanocomposite RVE

In order to conduct the pull-out simulations of a CNT from an epoxy matrix, an RVE was built to contain an SWCNT embedded at the center of the RVE and the epoxy polymer molecules. In the current MD simulations, periodic boundary conditions were applied in the x- and y-directions, while the z-direction was non-periodic and shrink-wrapped. The time step used in the MD simulations was selected to be 1 fs for all MD simulations, and a cutoff distance of 12 Å was used to model vdW interactions. The main steps involved in preparing both the uncured and cured epoxy composites are as follows:

Step 1–Volume reduction: Since Packmol software treats molecules as rigid bodies, the size of the RVE was initially enlarged to accommodate all the epoxy molecules and the CNT atoms. Subsequently, the RVE was compressed gradually through seven steps from its initial dimensions of $150 \times 150 \times 45$ Å to the targeted size of $50 \times 50 \times 42$ Å, resulting in the appropriate density of the RVE. At each stage, the CNT was "frozen," and the coordinates of the epoxy atoms were remapped to fit inside the compressed box. The potential energy of the compressed box was then minimized using the conjugate gradient method. The final compressed box is demonstrated in Fig. 3.8b.

Step 2–Equilibration: The compressed box was initially equilibrated for 2 ns in the isothermal-isobaric (NPT) ensemble at 300 K and 1 atm using the Nose–Hoover algorithm to evenly distribute the molecules due to the volume reduction. The equilibrium was ensured by using the following temperature cycle protocol. Two stepwise NPT cycles of heating and cooling (from 400 K to 300 K by a step of 25 K) were performed with each step occupying 10 ps. This was followed by a

simulation in the NPT ensemble for 1 ns at 300 K and 1 atm to generate an epoxy system with an appropriate CNT-matrix interfacial thickness. The final equilibrated density was found to be 0.94 g/cm^3, which is slightly less than expected due to the non-periodic boundary in the z-direction of the RVE.

3.2.3 Molecular Modeling of Compressive Load Simulation

3.2.3.1 Molecular Structure of CNTs with Defects

It is expected that defects have an influence on buckling behavior of CNTs, since buckling is very sensitive to geometric imperfections. However, it is crucial to understand the severity of the effect of different defects on the buckling behavior of CNTs. For CNTs with vacancy and SW defect, several factors can be presumed to influence buckling such as the number and location of defects, the number of vacancy clusters, and the distribution of these vacancy clusters. In order to examine the contribution of these factors, the defect configurations given in Fig. 3.9 are investigated. Specifically, vacancies coded as (1A), (2B), and (3A) are symmetric monovacancy, bivacancy, and trivacancy, respectively. Vacancies coded as (2C) and (2B) are asymmetric bivacancy and trivacancy, respectively. Both vacancies coded as (1B) and (1C) contain two monovacancies. The monovacancies (1B) locate exactly opposite to each other while the monovacancies (1C) locate towards one side of the nanotubes. Symmetric and asymmetric SW defects are coded as (1SW-A) and (1SW-B), respectively. Armchair (7, 7), (9, 9) and zigzag (12, 0) SWCNTs with the same aspect ratio of 6.5 were considered here. Two types of armchair SWCNTs were
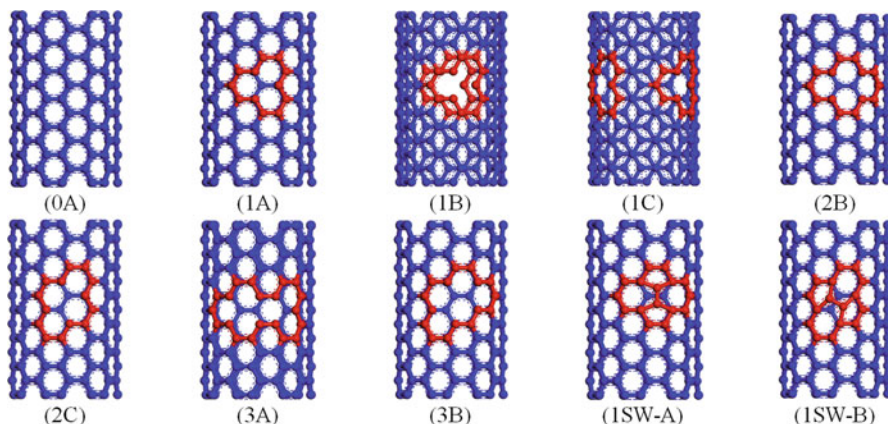
Fig. 3.9 Defects studied in this research (0A—pristine, 1A—monovacancy, 1B—two symmetrically distributed monovacancies, 1C—asymmetrically distributed two monovacancies, 2B—symmetric bivacancy, 2C—asymmetric bivacancy, 3A—symmetric trivacancy, 3B—asymmetric trivacancy, 1SW-A—symmetric SW defect, 1SW-B—asymmetric SW defect)

repeated to confirm the simulation results, and zigzag (12, 0) SWCNTs were chosen to have similar diameters to armchair (7, 7) SWCNTs. All defects were assumed to form onto the sidewall of SWCNTs. The defects were introduced approximately at the middle of the nanotubes since defects at the mid-length are proven to reduce buckling strain and buckling load to the greatest (Parvaneh et al. 2009; Wang et al. 2008).

3.2.3.2 Construction of Freestanding CNT and Nanocomposite RVE

It should be emphasized that the objective of the present chapter is to investigate the buckling behavior of an embedded CNT within a matrix and not the buckling behavior of the CNT-reinforced nanocomposites. Thus, both freestanding CNTs and CNT-epoxy nanocomposites were prepared here with the view to understand the influence of matrix material on the buckling of defective CNTs. To prepare freestanding armchair (7, 7), (9, 9) and zigzag (12, 0) SWCNTs for compression, the SWCNTs were initially minimized in terms of total potential energy using the conjugate gradient method. This was followed by canonical (NVT) equilibration at 300 K for the duration of 50 ps using a time step of 1 fs. The boundary condition was kept non-periodic in all three directions, and vdW interactions were truncated at a cutoff distance of 12 Å.

For the buckling simulation of embedded CNTs, the epoxy system was the same as the one for the pull-out analysis. In this MD simulation, periodic boundary conditions were applied in x- and y-directions, while periodicity was removed in z-direction. The time step used in the MD simulation was selected to be 1 fs, and a cutoff distance of 12 Å was used to model vdW interactions. The same parameters were followed for different RVEs containing different armchair (7, 7), (9, 9) and zigzag (12, 0) SWCNTs. For example, the main steps involved in preparing the buckling simulation for the (7, 7) pristine SWCNT-epoxy nanocomposites are as follows:

Step 1–Volume reduction: Since Packmol software treats molecules as rigid bodies, the size of the RVE was initially enlarged to accommodate all the epoxy molecules and the CNT atoms. Subsequently, the RVE was compressed gradually through seven steps from its initial dimensions of $150 \times 150 \times 62$ Å to the targeted size of $50 \times 50 \times 62$ Å, resulting in the appropriate density of the RVE. At each stage, the CNT was "frozen," and the coordinates of the epoxy atoms were remapped to fit inside the compressed box. The potential energy of the compressed box was then minimized using the conjugate gradient method.

Step 2–Equilibration: The compressed box was initially equilibrated for 2 ns in the isothermal-isobaric (NPT) ensemble at 300 K and 1 atm using the Nose–Hoover algorithm to distribute the molecules evenly due to the volume reduction. The equilibrium was ensured by using the following temperature cycle protocol. Two stepwise NPT cycles of heating and cooling (from 400 to 300 K by a step of 25 K) were performed with each step occupying 10 ps. This was followed by a simulation in the NPT ensemble for 1 ns at 300 K and 1 atm to generate an epoxy

system with the appropriate CNT-matrix interfacial thickness. The final equilibrated density of the SWCNT-epoxy RVE was found to be 0.95 g/cm^3, which is slightly less than expected due to the non-periodic boundary in the z-direction of the RVE.

3.3   Molecular Dynamics Simulation

3.3.1   Pull-Out Simulation

3.3.1.1   CNT Pull-Out Method

The MD pull-out numerical experiments were carried out to determine the ISS of the epoxy nanocomposite systems considered. In the existing pull-out studies, mainly two types of approaches are used to conduct MD pull-out simulations: the displacement pull-out approach (Chen et al. 2015; Li et al. 2011; Zheng et al. 2008, 2009) and the velocity pull-out approach (Wernik et al. 2012, Meguid et al. 2010; Wernik and Meguid 2011). For the displacement pull-out approach, the CNT is pulled out a certain distance. This is followed by an equilibration to ensure that the CNT-polymer system reaches equilibrium prior to the next CNT pull-out. This process is repeated until the CNT is completely out of the matrix. In terms of the velocity pull-out approach, the CNT is pulled out a small distance each step continuously until it is completely out of the matrix. Xiong and Meguid (2015) found that these two approaches produced very similar pull-out results if the simulation parameters were properly adjusted. Hence, in this chapter, we employed only the velocity pull-out approach, thanks to the less time spent on the MD simulations. In order to prevent the simultaneous drift of the epoxy with the CNT in the z-direction during the pull-out process, one edge of the epoxy molecules was constrained (shown in red in Fig. 3.10). The constrained system was further equilibrated in the NVT ensemble at 300 K for 50 ps to avoid the effect of the constraint on the final results. The composition of the RVE prior to the pull-out process of the pristine CNT is listed in Table 3.1. Subsequently, the edge atoms of the CNT, which are marked in green in Fig. 3.10, were pulled out at a uniform velocity of 1×10^{-4} Å/fs at 300 K in the NVT ensemble until the CNT was completely pulled out from the matrix. During the pull-out process, the driving forces formed by the CNT edge atoms pulled out the remaining CNT atoms in the z-direction. Since the interactive deformation of the CNT and the epoxy atoms were enabled, our method can accurately capture the effect of each defect and functionalization on the interfacial load transfer mechanisms in a deformable epoxy polymer matrix.
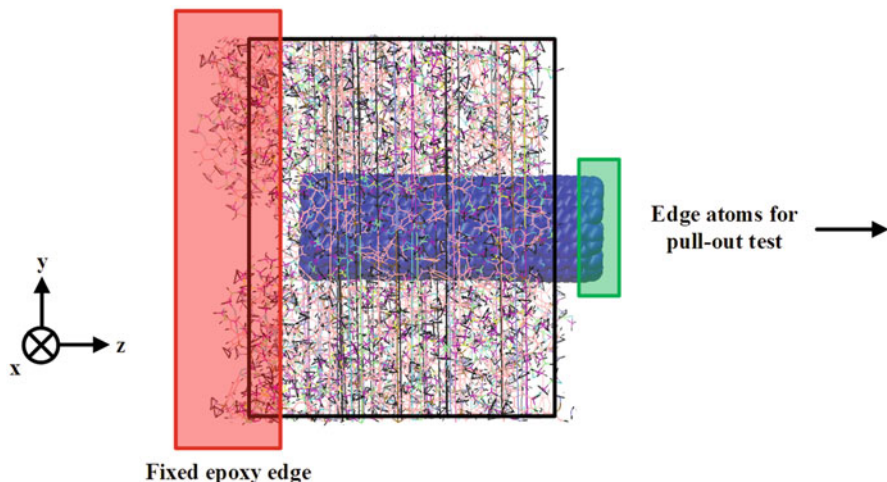
Fig. 3.10 Setup for pull-out simulation of a CNT from the epoxy matrix

**Table 3.1** Composition of nanocomposite RVE immediately before pristine CNT pull-out simulation

CNT			Epoxy	Composites				
Chiral vector	Length (Å)	Radius (Å)	No. of chain	X (Å)	Y (Å)	Z (Å)	Density (g/cm^3)	Total number of atoms
(9,9)	38.120	5.752	33	52.323	52.323	51.111	0.94	11,238

3.3.1.2 Evaluation of ISS

There are four theories in the literature regarding the location along the CNT where the ISS is the largest. Natsuki et al. (2007) and Zhang and Wang (2005) proposed that the ISS be the largest at the pull-out end of the CNT and decays nearly exponentially with the nanotube depth into the polymer (model A in Fig. 3.11a). In contrast, Gao and Li (2005) suggested that the maximum occurs at both ends of the CNT but that it is zero at the middle of the nanotube (model B in Fig. 3.11b). A similar method was used by Li et al. (2011), where they assumed that the ISS was distributed uniformly within 10 Å from each end of the CNT (model C in Fig. 3.11c). The most common assumption is that the ISS is uniformly distributed along the entire length of the CNT (Gou et al. 2004; Al-Ostaz et al. 2008) (model D in Fig. 3.11d).

In model A, the maximum ISS (τ), which occurs at the nanotube pull-out end, is given as (Cox 1952; Chua and Piggott 1985),

$$\tau = \frac{Fn}{2\pi r^2 \tanh(nL/r)} \tag{3.5}$$
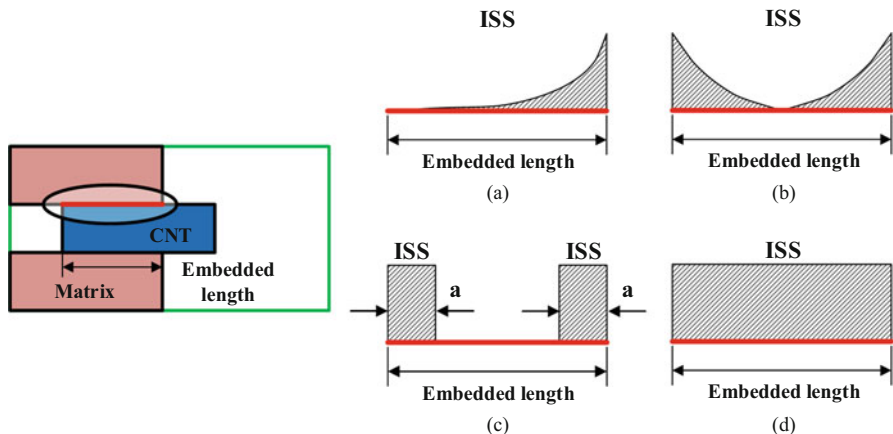
Fig. 3.11 Different proposed distribution of ISS: (**a**) exponential decay of ISS, (**b**) dominant ISS at CNT ends and decays rapidly, (**c**) uniform distribution of ISS near CNT ends, and (**d**) uniform ISS for the entire length of CNT

where F is the pull-out force, r is the radius of the CNT, L is the embedded initial length of the CNT into the matrix, n is a parameter given by $n = \sqrt{\frac{E_m}{E_{nt}(1+v_m)\log\left(\frac{t}{2r}\right)}}$, in which E_m is the polymer's Young's modulus, v_m is its Poisson's ratio, E_{nt} is the nanotube's Young's modulus, and t is the total thickness of the polymer film. Most numerical simulations used models C and D to estimate the ISS, since it is easy to calculate. In model C, the ISS is defined by,

$$\tau = \frac{F}{4\pi ra} \tag{3.6}$$

which assumes that the ISS is distributed at both ends of the CNT, and where a is the length along the CNT over which the ISS is distributed.

For model D, there are two approaches: force approach and energy approach, to calculate the ISS in the literature. In terms of the force approach, the ISS can be calculated from the pull-out force, as follows:

$$\tau = \frac{F}{2\pi rL} \tag{3.7}$$

The energy approach adopted in Gou et al. (2005), Zheng et al. (2009) and Yang et al. (2015) is the most common approach used to predict the ISS of CNT-reinforced composites. Since the work required to pull the CNT out is attributed to the shear force between the CNT and the matrix, the ISS can be calculated from the pull-out work ($W_{pull-out}$), as follows:

$$W_{pull-out} = \int_0^L 2\pi r \left(L - z\right) \tau_i dz = \pi r L^2 \tau \qquad (3.8)$$

where z is the pull-out distance from the initial position to the final position of the CNT.

Hence, in this chapter, we will adopt the energy approach to estimate the ISS. The pull-out work is usually defined as the variations in the potential energy of the entire system after and prior to the pull-out process, as follows:

$$W_{pull-out} = E_{potential}^{final} - E_{potential}^{initial} \qquad (3.9)$$

The potential energy of the nanocomposite can be described as follows:

$$E_{total} = E_{cnt} + E_{epoxy} + E_{interaction} \qquad (3.10)$$

where E_{cnt}, E_{epoxy}, and $E_{interaction}$ are the potential energy of the CNT and epoxy as well as the interaction energy between the CNT and epoxy matrix, respectively. However, some researchers (Zheng et al. 2008, 2009; Yang et al. 2015; Jang et al. 2013) argue that the change in the total potential energy includes both the potential energy variations of the CNT and the epoxy which do not contribute to the calculation of ISS. Therefore, in order to obtain more accurate and reliable ISS, the change in the CNT–matrix interaction energy is considered as the pull-out work, as follows:

$$W_{pull-out} = E_{interaction}^{change} = E_{interaction}^{final} - E_{interaction}^{initial} \qquad (3.11)$$

Both of these pull-out work definitions are used to calculate the ISS, and their application conditions are discussed in this chapter. Since most of the atoms in the CNTs are electrically neutral and there are no bonded interactions between the CNT and the matrix, the CNT–matrix interaction energy is mostly attributed to non-bonded vdW interactions. Several researchers (Gou et al. 2004, 2005) also determined the interfacial binding energy γ between a CNT and the matrix which serves as another reliable indicator of the effect of defects and functionalization on the nanocomposites. The interfacial binding energy γ per unit area can be obtained from the interaction energy ($E_{interaction}$) scaled by twice the instantaneous contact area,

$$\gamma = \frac{E_{interaction}}{2A} \qquad (3.12)$$

where A is the instantaneous contact area at each pull-out step.

Since the dimensional changes of CNTs containing defects and functional groups influence the ISS, the diameter and length of defective and functionalized CNTs

Table 3.2 Equilibrium length and radius of CNTs according to different types and numbers of modified sites

Defect type	No. of defects	300 K	
		Radius (Å)	Length (Å)
Pristine		5.752	38.120
Monovacancy	3	5.756	38.208
	6	5.762	38.297
	9	5.775	38.345
	12	5.776	38.466
	15	5.794	38.507
	18	5.799	38.612
Bivacancy	2	5.758	38.197
	3	5.752	38.201
	4	5.750	38.254
	5	5.754	38.253
	6	5.762	38.254
	7	5.763	38.267
	8	5.769	38.308
	9	5.782	38.323
Trivacancy	1	5.758	38.146
	2	5.754	38.122
	3	5.749	38.272
	4	5.757	38.229
	5	5.761	38.245
	6	5.761	38.183
Adatom	4	5.761	38.187
	8	5.772	38.258
	12	5.780	38.313
SW	5	5.758	38.071
	10	5.743	38.091
	15	5.758	38.006
Phenyl group	3	5.760	38.230
	6	5.759	38.156
	9	5.766	38.182

after the equilibration of epoxy systems were used in all of our MD simulations. The new averaged dimensions of CNTs are summarized in Table 3.2. Compared with the pristine CNT, only the length of SW defective CNT decreases, whereas the diameter and length of other CNTs increase.
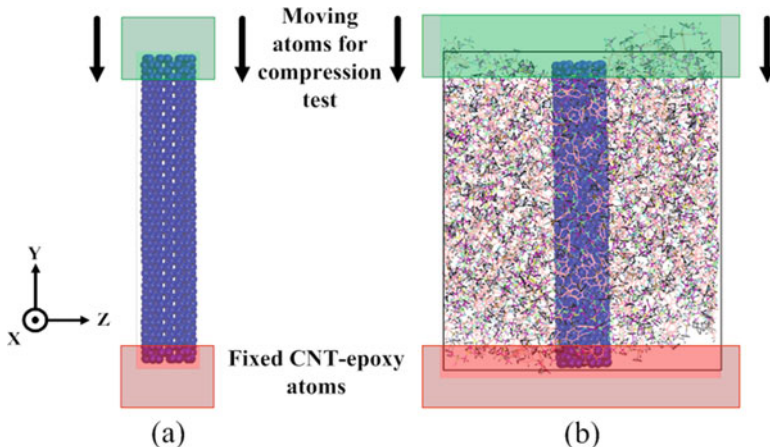
Fig. 3.12 Setup for the buckling simulations of (**a**) freestanding SWCNT, and (**b**) SWCNT embedded in the epoxy matrix

3.3.2 Compressive Load Simulation

#### 3.3.2.1 CNT and RVE Compressive Load Method

The MD compression simulations were carried out to determine the critical buckling strain and buckling load of both freestanding SWCNTs and SWCNT-epoxy nanocomposite systems. To prevent the simultaneous drift of the SWCNT and epoxy atoms in the z-direction during the compression process, we constrained one end of the freestanding SWCNT and the RVE (shown in red in Fig. 3.12). In order to avoid the effect of the constraint on the final results, the constrained systems were further equilibrated in the NVT ensemble at 300 K for 50 ps. The composition of the freestanding SWCNTs and RVEs containing different SWCNTs prior to the compression process is listed in Table 3.3. After the equilibration was complete, an incremental displacement of 0.01 Å was applied on the other end of the freestanding SWCNTs and RVEs, which are marked in green in Fig. 3.12. After each increment, the systems were relaxed for a period to achieve a new equilibrium state while keeping the two ends constrained. The loading was repeated at 300 K in the NVT ensemble until the buckling occurred. Similar to the pull-out simulation, our method can capture the effect of each defect accurately on the buckling behavior of CNTs embedded in a deformable epoxy polymer matrix.

3.3.2.2 Evaluation of Buckling Behavior

As for the assessment of buckling behavior, the strain energy-strain and force-displacement curves for the pristine SWCNTs are shown in Fig. 3.13a, b, respec-

Table 3.3 Composition of freestanding SWCNTs and RVEs containing different SWCNTs immediately before compression simulations

SWCNT			Epoxy	Composites				
Chiral vector	Length (Å)	Radius (Å)	No. of chain	X (Å)	Y (Å)	Z (Å)	Density (g/cm^3)	Total number of atoms
(7, 7)	55.89	4.46	–	–	–	–	–	700
(9, 9)	72.11	5.73	–	–	–	–	–	1152
(12, 0)	56.68	4.39	–	–	–	–	–	696
(7, 7)	55.47	4.48	44	52.47	52.47	66.79	0.95	14,868
(9, 9)	71.70	5.75	57	52.21	52.21	87.05	0.97	19,506
(12, 0)	55.97	4.45	44	52.47	52.47	67.12	0.94	14,864
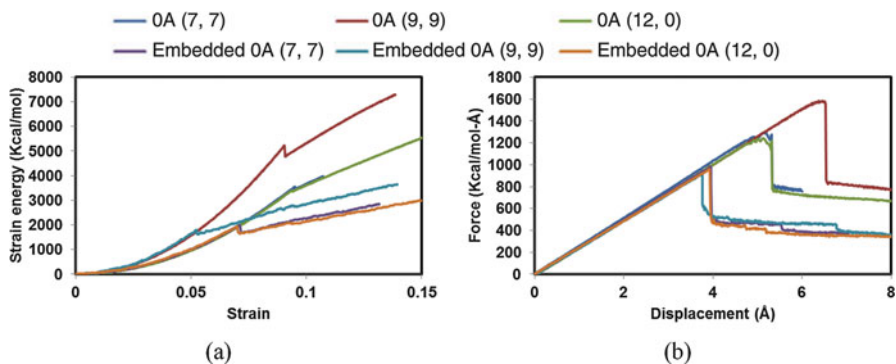
Fig. 3.13 (**a**) Strain energy-strain curves; (**b**) force-displacement curves for different pristine freestanding and embedded SWCNTs

tively. The critical buckling state is detected by a sudden drop of strain energy or force. This sudden drop is associated with significant structural and geometrical changes of CNTs (shown in Fig. 3.14) corresponding to the release of energy in CNTs. It can be seen in Fig. 3.14 that different pristine SWCNTs with an aspect ratio of 6.5 buckle sideway with the occurrence of a flattening at the center, which is recognized in the literature as being "beam-shell buckling mode." It is a mixture of globalized beam-like buckling for a long and slender CNT and localized shell-like buckling within the atomic layer of a short CNT. In agreement with the findings of Wang et al. (2010, 2014), we conclude that CNTs with aspect ratios more than 6 exhibit beam-shell buckling mode, such as a single beam while preserving its circular cross section with localized shell buckling within the atomic layer. From Fig. 3.13a, it is observed that the strain energy can be approximately expressed as a quadric function of the strain before the singularity happens in each curve, viz.:

$$U = \frac{1}{2}EAL\varepsilon^2 \qquad (3.13)$$
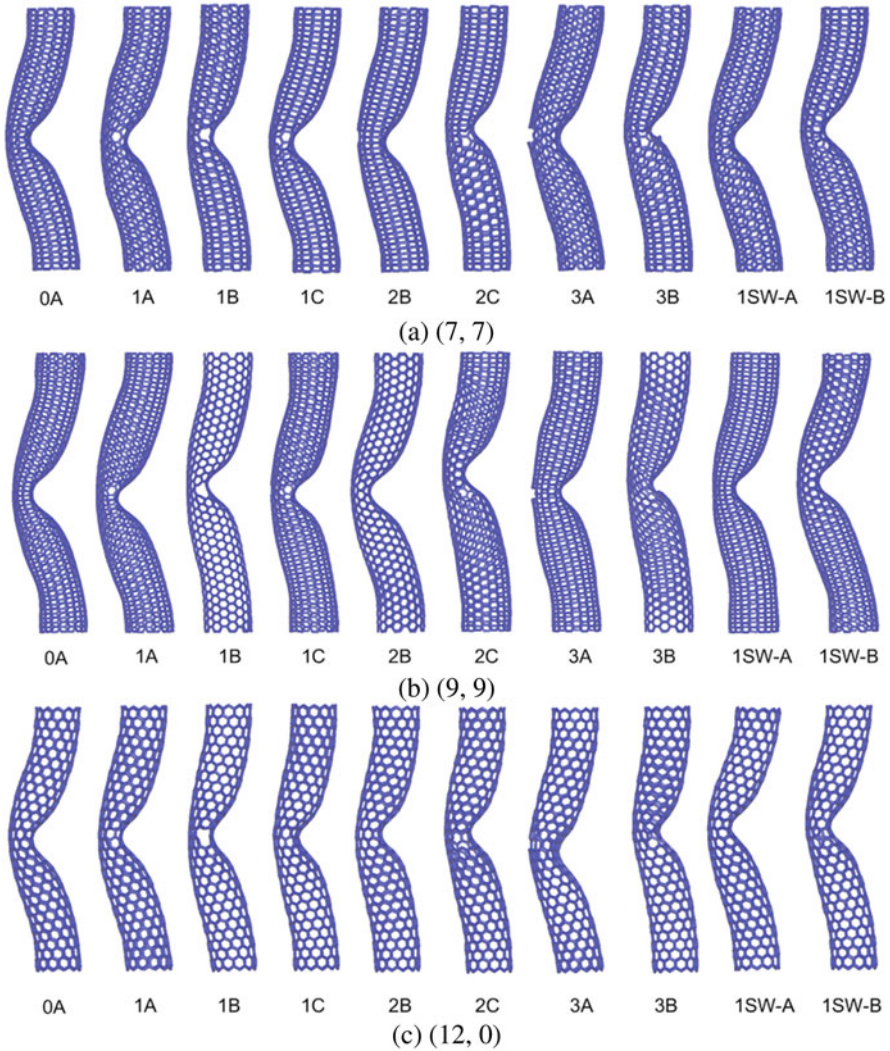
Fig. 3.14 Buckling mode shapes of the freestanding SWCNTs (**a**) (7, 7), (**b**) (9, 9), and (**c**) (12, 0)

where U, E, A, L, and ε are the strain energy, Young's modulus, cross-sectional area, original length, and strain of the nanotubes, respectively. This indicates that the SWCNTs sustain elastic deformation under a compressive force in accordance with Hooke's law until bifurcation. Note that in Fig. 3.13a the critical buckling strain is defined as the strain at which the strain energy of the simulated SWCNT registers its first sudden drop in value. We can also see in Fig. 3.13b that the compressive force which the SWCNTs can withstand increases almost linearly with the axial

displacement until the buckling load is reached. Accordingly, this relationship can be formulated as

$$F = \frac{EA}{L}\Delta L \tag{3.14}$$

where F is the compressive force and ΔL is the end-shortening displacement. As it is shown in Fig. 3.13b, there are two values of axial load P at the critical buckling state. The upper value of P at the critical buckling state is defined as the critical buckling load P_{cr} and the corresponding end-shortening displacement is defined as the critical buckling displacement Δ_{cr}. Coincident with the value obtained through strain energy, the critical buckling strain ε_{cr} can also be calculated by dividing Δ_{cr} with the original length L of CNT.

3.4   Results and Discussions

3.4.1   Analysis of Pull-Out Simulation

3.4.1.1   MD Model Validation

Figure 3.15 shows a snapshot of the respective pull-out process of a pristine CNT from uncured and cured epoxy matrices. We can see that debonding takes place among the uncured epoxy molecules in close proximity to the CNT-matrix interfaces, and that a substantial number of uncured epoxy molecules are attached to the CNT. However, in the cured case, no epoxy molecules are pulled out along
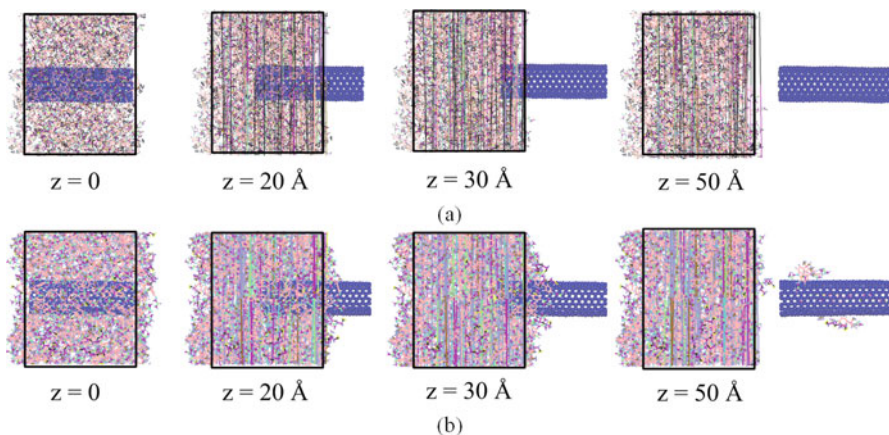
Fig. 3.15 Schematics of the pull-out processes of pristine CNT embedded in (**a**) uncured epoxy matrix and (**b**) cured epoxy matrix
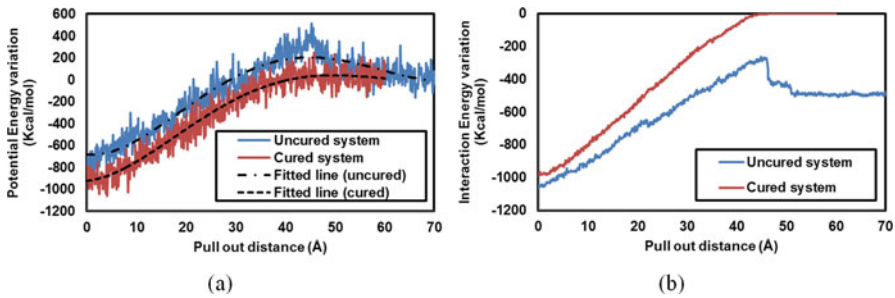
Fig. 3.16 (**a**) Potential energy and (**b**) interaction energy variations in pristine CNT with pull-out distance

with the CNT. The respective variations in the total potential energy and interaction energy of the uncured and cured CNT-epoxy systems are shown in Fig. 3.16. The zero point of the potential energy is taken as the position where the CNT is pulled out from the matrix completely. Note that the fluctuation in the potential energy of the system is attributed to the rearrangement of molecules in the RVE, and they are fitted using dashed polynomial curves. It can be observed from Fig. 3.16a that the potential energy of the cured system changes from approximately −1000 Kcal/mol to zero at full pull-out, while the corresponding uncured system changes from approximately −700 Kcal/mol to zero again at full pull-out of the CNT from the matrix. This is because the pull-out work is transferred into an increase in the potential energy of the system as the pull-out process proceeds. The reduced level of the change in potential energy of the uncured system can be explained in Fig. 3.15a. The figure shows that some of the uncured molecules are attracted back to the RVE due to vdW forces. And, this happens before the CNT is pulled out completely from the matrix. Since no epoxy molecules are pulled out from the cured epoxy system, the potential energy of the matrix and CNT remains almost constant. This is demonstrated by the very similar variation in the interaction energy of the cured system in Fig. 3.16b. We can also see in Fig. 3.16b that the initial interaction energy magnitude of the uncured system is larger than that of the cured one. However, the final interaction energy of the uncured system does not change to zero as some epoxy molecules are attached on the pull-out CNT.

Based on the change in the total potential energy, the ISS of the uncured and cured epoxy composites was determined to be 198 and 250 MPa, respectively. The higher ISS of the cured system is because the epoxy resin is strengthened by the crosslinked structures developed during the curing process. Since the CNT does not interact with the epoxy matrix after the CNT is pulled out completely, the change in the interaction energy is equal to the initial CNT–matrix interaction energy. By applying the initial interaction energy, we found that the ISS of cured systems is very similar to the ISS based on the total potential energy. However, the ISS of the uncured system becomes 277 MPa, which is unreasonably high because it ignores the energy expended in deforming the polymer during the pull-out test. Thus, we

decide to use the determination based on the total potential energy to calculate the ISS accurately while keeping the ISS based on the initial interaction energy for comparison. The current ISS estimates for the pristine CNTs were found to be in good agreement with those of existing MD pull-out studies with some minor discrepancies due to the use of the different forcefields used in the simulations. For instance, Bohlén and Bolton (2013) used COMPASS forcefield to calculate the ISS via a new approach which assumed that the ISS was distributed uniformly within 10 Å from each end of the SWCNT, but was zero at the middle of the nanotube. The ISS of an SWCNT-polyvinylidene fluoride system resulting from their approach was found to be 214.4 MPa compared with 250 MPa from the current chapter. Chowdhury and Okabe (2007) used MD simulations to examine the effect of polymer matrix density on the ISS. The carbon–carbon interaction in the CNT was modeled using Brenner potential while AMBER potential was used for the polymer matrix. The ISS was calculated to be 245 MPa for an SWCNT-PE composite with a density of 0.97 g/cm^3. Chowdhury et al. (2010) then used the same potential to study the effect of vacancy defects on the ISS of SWCNT-PE composites. They reported ISS reaching 300 MPa for a nanocomposite reinforced with pristine SWCNTs.

Figure 3.17 shows the relative concentrations of all atoms and sp^2 aromatic carbon atoms monitored as a function of the distance from the center of the CNT before and after crosslinking. We can see in Fig. 3.17a that the relative concentration of all atoms for the uncured matrix near the CNT is higher than the cured one. The increase in the relative concentration is because a less crosslinked structure allows more conformational freedom for the matrix to interact favorably with the CNT. Enhanced conformational flexibility allows a more favorable and denser packing of matrix atoms with the CNT. Moreover, Fig. 3.17b reveals that it is the relative concentration of the sp^2 carbon atoms that plays a major role in the CNT–matrix interaction energy. Such factors can improve the initial interaction energy at the CNT-epoxy interface, leading to overestimation of the ISS of the uncured system. Figure 3.18 compares the aromatic ring distribution near the CNT in the uncured
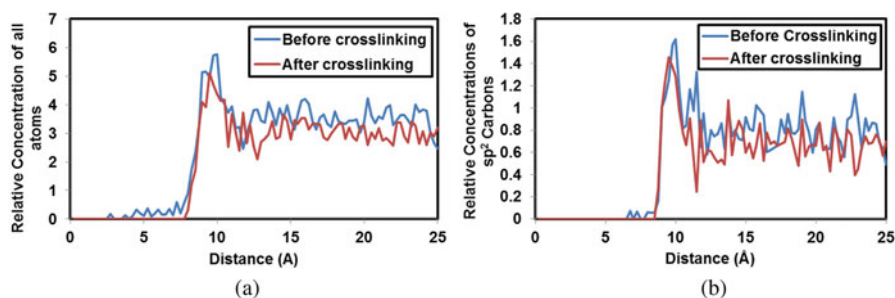
Fig. 3.17 Spatially averaged concentration profiles versus distance from the center of the CNT before and after curing to 50% conversion (**a**) for all atoms and (**b**) for sp^2-hybridized carbon atoms
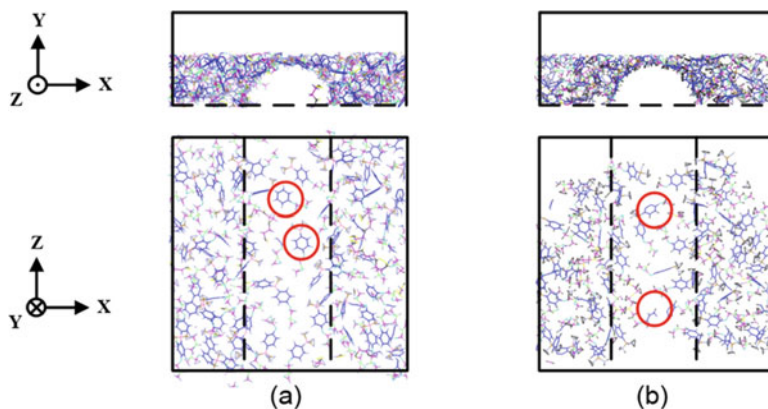
Fig. 3.18 Aromatic ring distribution near the CNT in (**a**) uncured epoxy matrix and (**b**) cured epoxy matrix

and cured systems schematically. The red circles highlight typical aromatic ring conformation near the CNTs. We can see that aromatic rings in the uncured epoxy matrix are preferentially aligned parallel to the surface of the CNT, which optimizes π-stacking. The curing of the epoxy matrix sterically works against the aromatic rings lying flat on the surface of the CNT, reducing the interaction energy induced by π–π attractions at the CNT-epoxy interface. This chapter examines the relative concentration of the sp^2 carbon atoms to investigate the resulting interface properties better.

3.4.1.2 Effect of Vacancy Defects upon ISS

The variations in the ISS of uncured and cured nanocomposite systems containing a defective CNT with different numbers of missing atoms are depicted in Fig. 3.19. This figure reveals that the ISS of the cured systems decreases as the number of missing atoms in the CNTs increases irrespective of the type of these defects. Since the potential energy of the epoxy and CNT does not alter very much for the cured systems, the interaction energy becomes the major contributor to the ISS. The vdW interaction between the CNT and the matrix solely contributes to the interfacial interaction energy. Thus, and as expected, the vdW interaction energy is reduced as a result of increasing number of vacancy defects in the CNT, which will eventually degrade the ISS. From Fig. 3.20a–c, it is clear that the relative concentrations of sp^2 carbon atoms near the CNT decrease with the increase in the number of vacancy defects irrespective of the type of defect. An increasing number of vacancy defects decreases the number of sp^2 carbon atoms in the CNT, which in turn reduces the ISS induced by π–π attractions. Unlike the cured systems, Fig. 3.19 shows that the number of vacancies in the uncured systems does not affect the ISS. This observation can be explained by the very low shear strength in the uncured
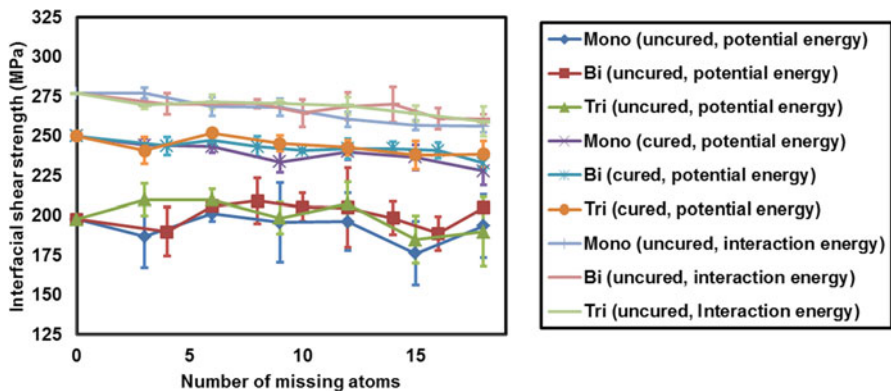
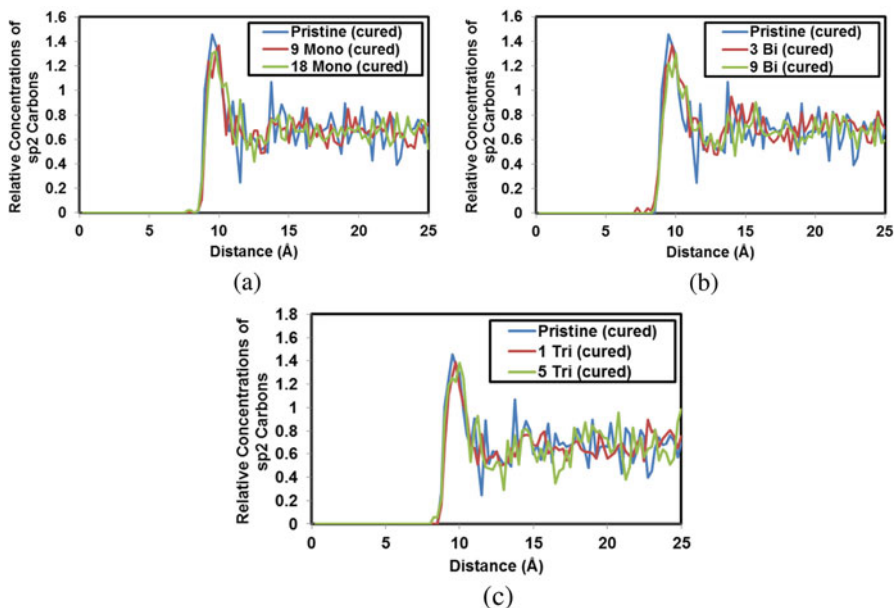**Fig. 3.19** Variations in ISS with number of missing atoms

Fig. 3.20 Relative concentrations of sp^2 carbon atoms for (**a**) different monovacancies after curing, (**b**) different bivacancies after curing, and (**c**) different trivacancies after curing

systems. Similar to the uncured pristine CNT system, the debonding takes place initially among the epoxy molecules near the CNT-matrix interface during the pull-out process. Therefore, it is predominantly the uncured epoxy molecules rather than the CNT-epoxy interface that governs the shear strength of the interface. In addition, based on the initial interaction energy, the ISS of the uncured systems in Fig. 3.19 is unreasonably higher than the ISS of the cured systems due to the ignorance of the matrix deformation energy.

Our results in Fig. 3.19 also reveal that for the same number of missing atoms, different types of vacancy defects have almost the same effect on the ISS of the cured systems. We can see that the ISS for various types of vacancies decline at a similar rate and are overlapped for the most part of the curves. Therefore, it can be deduced that the decrease in the ISS is independent of the defect type. The fluctuation of the ISS is possibly due to the different distribution of vacancies within the CNTs and the surrounding epoxy molecules. A total of 18 missing atoms were considered in this chapter, and the average maximum percentage of decrease in the ISS of the cured epoxy matrix was found to be 7.0%.

Our findings generally agree with the earlier work of Yang et al. (2015), but their work used COMPASS forcefield to study SWCNTs embedded in thermoplastic (PE) systems with no crosslinked structures. They reported 4.71% reduction of the ISS for 9 missing atoms. Chowdhury et al. (2010) examined three patterns of vacancy defects with different sizes and distributions; considering up to 8 missing atoms. They found a maximum reduction in ISS of about 5.33%, 5.00%, and 6.00% for one-atom, two-atom, and line vacancies, respectively. Furthermore, the weakened interfacial load transfer ability at the nanotube-matrix interface often leads to a decrease in mechanical properties of nanocomposites. For instance, Xiao and Hou (2006) used MD simulations to investigate the effect of a two-atom vacancy defect on the fracture of CNT-aluminum(AL) composites. As compared with pristine CNT-AL composites, the fracture stress and fracture strain of defected CNT-AL composites reduced by 36% and 57%, respectively. In general, it was found that defected CNT with a small volume fraction cannot reinforce but instead weaken nanocomposite materials. Joshi et al. (2011) investigated the effect of pinhole defects on mechanical properties of wavy CNT-based nanocomposites using RVE as well as Halpin–Tsai equations. They observed that the presence of 7 pinhole defects with each containing 24 atoms on a wavy nanotube can reduce the longitudinal elasticity modulus of the composite by 0.93% when compared with CNT without pinhole defects, and the elasticity modulus decreases with the increase in the number of pinhole defects. Sharma et al. (2014) used MD simulations to study the effects of vacancy defects on SWCNT-polypropylene composites. Results showed that one vacancy defect with 16% SWCNT volume fraction reduces both Young's modulus and shear modulus by 13% and 34%, respectively.

Figure 3.21 exhibits the interfacial binding energy of cured epoxy systems for the respective monovacancy, bivacancy, and trivacancy defects in CNTs obtained from the CNT–matrix interaction energy divided by twice the instantaneous contact area, as defined in Eq. (3.12). In all cases, the magnitude of interfacial binding energy increases gradually as the CNT is pulled out from the matrix. The increase in the interfacial binding energy is due to the reduction in the contact area between the CNT and matrix during the pull-out process. Furthermore, it can be observed that the magnitudes of the interfacial binding energies in the case of vacancy defects in CNTs are initially smaller and then exceed that of pristine CNTs as the pull-out distance of the CNT increases. The snapshots of the pull-out process depicted in Fig. 3.22 reveal that some of the epoxy molecules entered in the vacancy defective CNT
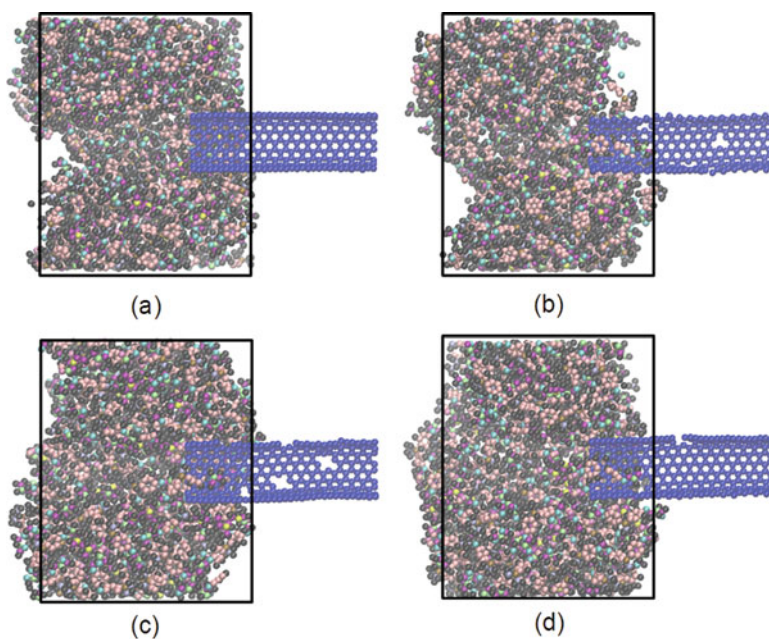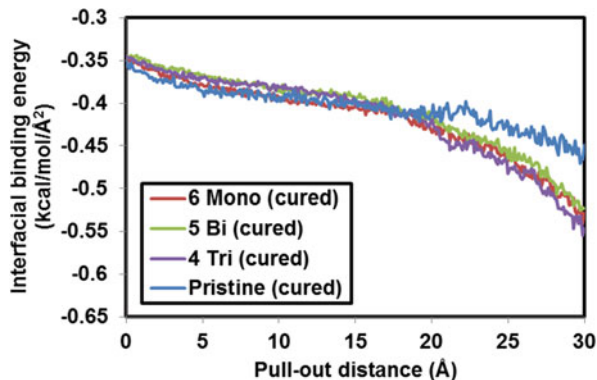
Fig. 3.22 Cross sections of the pull-out processes for pristine and vacancy defective CNT in cured epoxy matrix at z = 30 Å: (**a**) pristine, (**b**) 6 monovacancy, (**c**) 10 bivacancy, and (**d**) 12 trivacancy

through their uncapped ends, leading to the enhancement of the interaction energy during the pull-out process. This results in a prominent increase in the interfacial binding energy of vacancy defective CNT during the pull-out process.
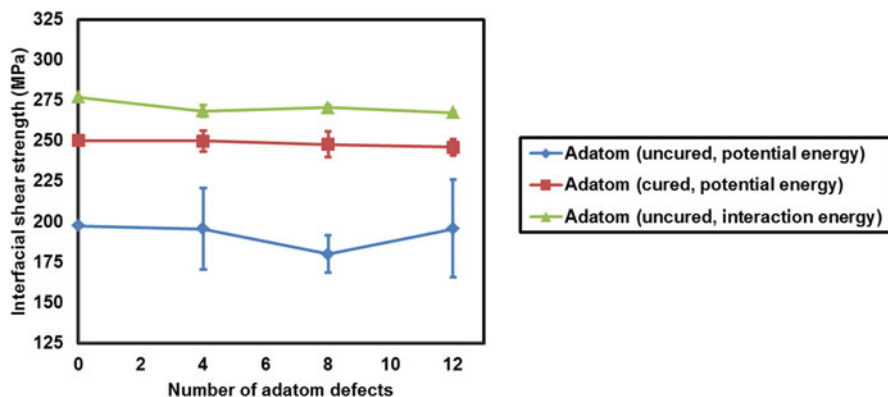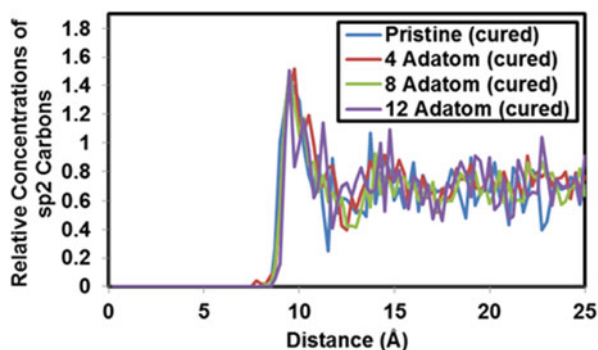
Fig. 3.23 Variation in ISS with number of adatom defects

Fig. 3.24 Relative concentrations of sp^2 carbon atoms for different adatoms after curing


3.4.1.3 Effect of Carbon Adatom upon ISS

Unlike the cured cases of vacancy defects, adatom defects have only marginal influence on the ISS of the cured epoxy composites, as depicted in Fig. 3.23. This observation can be explained in terms of the rehybridization and the total number of carbon atoms in the adatom defective CNTs. Newly introduced carbon atoms rehybridize the adjacent carbon atoms and replace 2 sp^2 by 3 sp^3 carbon atoms. Although adatom defective CNTs have more carbon atoms, the unchanged ISS indicates that the interaction energy due to 3 sp^3 carbon atoms is similar to that due to 2 sp^2 carbon atoms. As showed in Fig. 3.24, the concentrations of sp^2 carbons are almost the same for different number of adatoms in the cured matrix. This also helps to shed light on the marginal influence of adatom defects. Additionally, it is evident from Fig. 3.23 that adatom defective CNTs embedded in the uncured system have very similar ISS, which is analogous to the uncured case of vacancy defects. We can also see that, without considering the matrix deformation energy, the method using the interaction energy still overestimates the ISS as expected.

Fig. 3.25 Variation in interfacial binding energy between adatom defective CNTs and cured epoxy matrix with pull-out distance
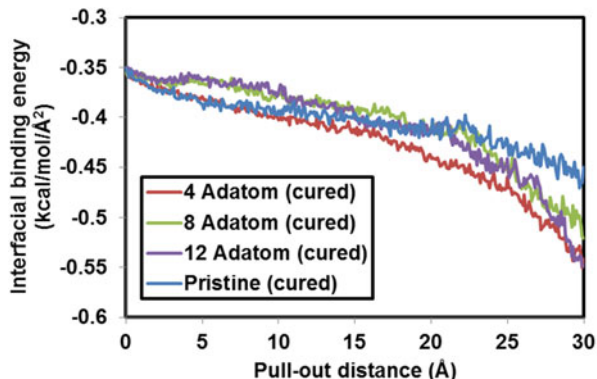
Our results are generally consistent with those reported by Yang et al. (2015), but their studies focused on thermoplastic (PE) systems without crosslinked structures. They found that adatom defects marginally increase the ISS by 1.14%, and they further demonstrated that the PE molecules are more effectively adsorbed on the sidewall of the adatom defective CNT than on the pristine CNT. Other researchers also studied the effect of other types of interstitial atoms on nanocomposites. For instance, Pavia and Curtin (2011) used MD simulations of a pull-out test to investigate the degree of interfacial coupling/adhesion between diamond matrix and CNTs. The interfacial behavior was captured using modified REBO potential through interstitial carbon atoms located in the interface, which can form and break bonds with both the matrix and CNT atoms. The total friction force is directly proportional to the number of interstitial carbon atoms along the interface, and the frictional stresses are high, reaching several GPa. Hence, the composite strength and toughness of such materials are expected to be greatly improved relative to materials with no covalent bonds at the interface. Pavia and Curtin (2013) further studied the response of CNT and interface to the matrix crack impingement as a function of the interface strength influenced by the number of interstitial carbon atoms. They simulated an annular crack propagating through a diamond matrix and impinging on the interface with a pristine SWCNT and DWCNT. The results showed that weaker interfaces fail in shear, while stronger interfaces do not fail, and instead the CNT fails once the stress acting on the CNT reaches its tensile strength. The transition from interface debonding to CNT fracture was found to depend on the interface and CNT strength.

Figure 3.25 shows the variations in the interfacial binding energies with the pull-out distance for the cured epoxy matrix. Analogous to the case of vacancy defects, the interfacial binding energies increase with the increase in the pull-out distance, and they further exceed that of pristine CNTs for larger pull-out distances. The prominent increase in the interfacial binding energy can be explained by the fact that carbon adatoms on the sidewalls of the CNTs act like a spike, protruding in the surrounding epoxy molecules, which tends to pull out epoxy molecules of the RVE during the pull-out process, as shown in Fig. 3.26.

Fig. 3.26 Cross section of
the pull-out process for 12
adatom defective CNT in
cured epoxy matrix at
z = 30 Å
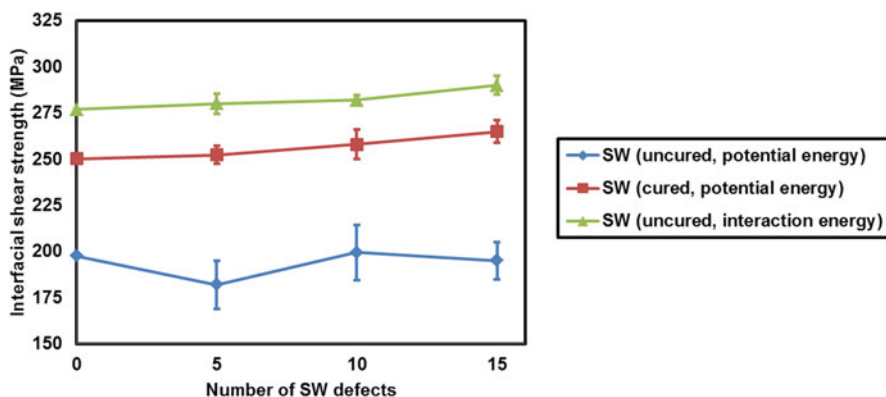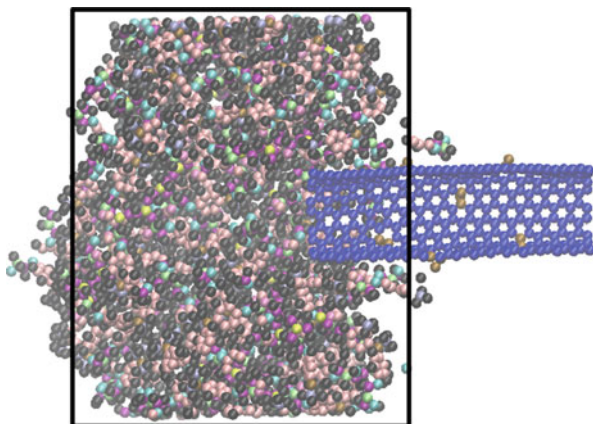
Fig. 3.27 Variation in ISS with number of SW defects

3.4.1.4 Effect of SW Defect upon ISS

In contrast to the vacancy and adatom defects, the ISS of epoxy nanocomposite
reinforced with CNTs containing SW defects increases as the number of SW
defects increases for the cured epoxy systems, as depicted in Fig. 3.27. Note
that the formation of SW defect involves neither missing carbon atoms nor the
rehybridization of these atoms in the CNTs. In this case, four hexagons are
transformed into two pentagons and two heptagons for a single SW defect. It may
be observed from Fig. 3.27 that the increase in the ISS of the cured systems is
6.0%. Since the growth in the number of SW defects increases the concentrations
of sp^2 carbons near the CNT (Fig. 3.28), it can be concluded that the increase in
the ISS results from the increase in $\pi-\pi$ attractions at the CNT-matrix interface. In
addition, the ISS in the uncured matrix tends to be unvaried. This again is caused by
the relatively low shear strength of the uncured epoxy systems. Due to the lack

Fig. 3.28 Relative concentrations of sp^2 carbon atoms for different SW defects after curing
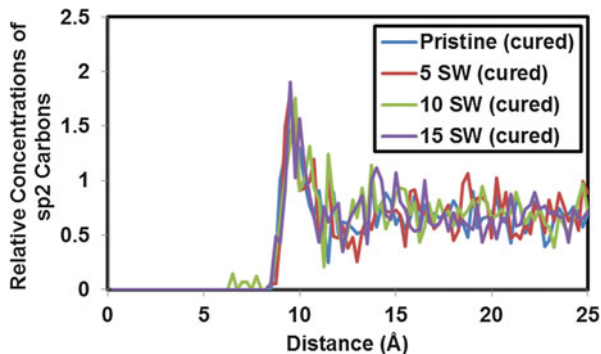

of the energy expended in deforming the polymer during the pull-out test, it is expected that the ISS based on the interaction energy for the uncured systems is again overestimated in Fig. 3.27.

Our results are in agreement with the observation made by Yang et al. (2015), though their work was concerned with thermoplastic (PE). They studied the effect of SW defects on the ISS of SWCNT-PE composite and found that the percentage increase in the ISS ranged from 0.71% to 7.14%. Zhou and Shi (2003) helped to explain the increase in the ISS by using a first-principle discrete variational method to estimate the binding energy of foreign atoms attached to CNTs with and without an SW defect. They found that SW defective CNT improves the binding energy magnitude by about 0.5 eV for some foreign atoms compared with the pristine CNT. This would improve the adsorption of the polymer matrix onto the CNTs. However, the overall mechanical properties of SW defective CNT-reinforced composites degrade, since SW defects reduce the mechanical properties of CNTs. For instance, Mahboob and Islam (2013) studied the effect of SW defects on the mechanical properties of composites reinforced with SWCNTs using MD simulations. Their results showed that the longitudinal Young's modulus of the SWCNT-PE composites is strongly dependent on the number of SW defects and CNT volume fraction. They found that SW defects reduce the longitudinal Young's modulus of the SWCNT-PE composites by 12%. Sharma et al. (2014) also used MD simulations to investigate the effect of SW defects on the elastic stiffness of CNT-PP composites. They found that the percentage decrease in moduli is greater for CNTs with SW defects in comparison to vacancy defective CNTs, and one SW defect with 16% SWCNT volume fraction decreases both Young's modulus and shear modulus by 16% and 44%, respectively.

Figure 3.29 shows the variations in the interfacial binding energies for the SW defective CNTs in the cured epoxy matrix against the CNT pull-out distance. Unlike the vacancy and adatom defective cases, the magnitudes of the interfacial binding energies of this case are larger than that of the pristine CNTs, and the energy difference increases with the increase in the pull-out distance. This is attributed to the stronger adhesion effect of SW defective CNTs. Figure 3.30 shows the cross section of the cured CNT-epoxy nanocomposite. It can be observed from Fig. 3.30

Fig. 3.29 Variation in interfacial binding energy between SW defective CNTs and cured epoxy matrix with pull-out distance
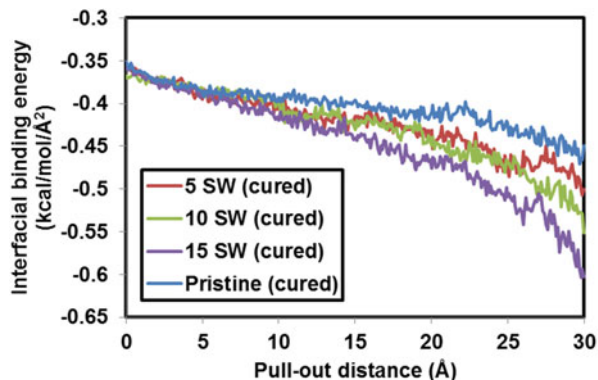
Fig. 3.30 Cross section of the pull-out process for 12 SW defective CNT in cured epoxy matrix at z = 30 Å
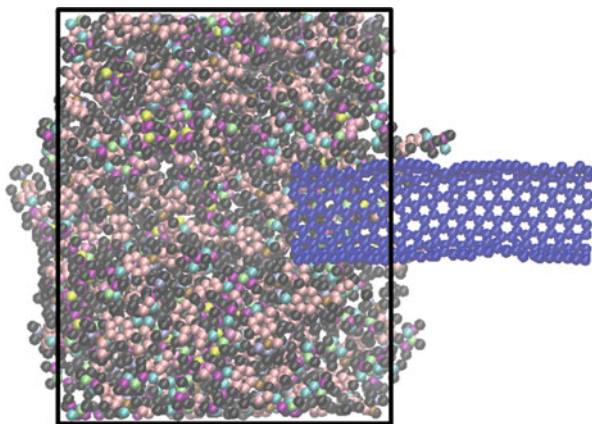
that some epoxy molecules adjacent to the sidewall of SW defective CNT are pulled out together with the CNT leading to an enhanced CNT–matrix interaction energy. This increase in the interaction energy leads to the increased interfacial binding energy difference between SW defective and pristine CNTs.

3.4.1.5 Effect of Phenyl Functional Group upon ISS

In this section, we establish the effect of functionalization on the ISS of CNT-epoxy nanocomposites. Figure 3.31 shows that the ISS increases dramatically with the increase in the number of the phenyl group functionalization on the sidewalls of the CNTs for the cured epoxy composites. Noteworthy is the fact that the carbon atoms of the CNTs are directly bonded to the phenyl group which changes the hybridization from sp^2 to sp^3, and this formation of the phenyl group functionalization adds more atoms to the original CNTs. Moreover, Fig. 3.32 shows that the relative concentrations of sp^2 carbons increase as the number of phenyl groups increases. This also results in the increase in the ISS induced by
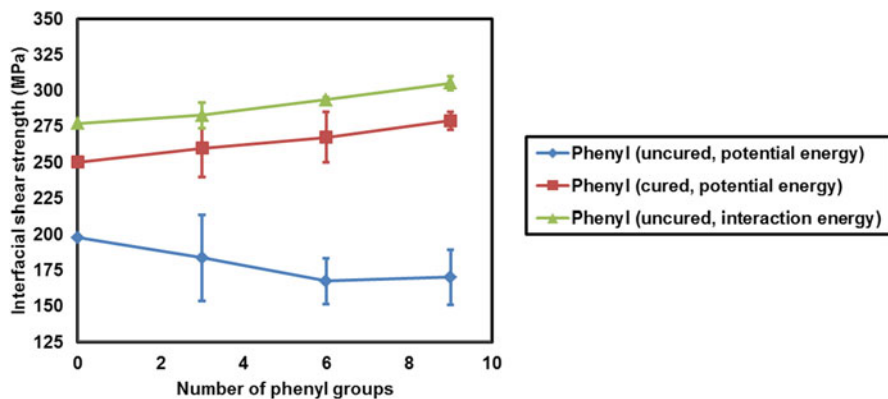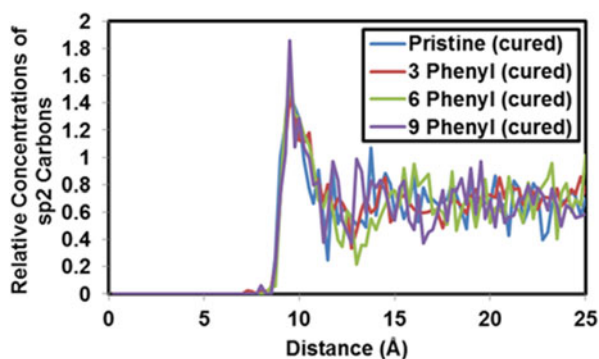
Fig. 3.31 Variation in ISS with number of phenyl groups

Fig. 3.32 Relative concentrations of sp^2 carbon atoms for different phenyl groups after curing

Ω–Ω attractions. Therefore, the increased ISS is mainly attributed to the additional vdW interactions between the attached phenyl groups and the epoxy molecules. Unsurprisingly, phenyl functional groups do not improve the ISS of the uncured systems due to the same reasons mentioned above. As expected in Fig. 3.31, the negligence of the matrix deformation energy for the uncured systems results in the overestimation of ISS.

It can be observed from Fig. 3.31 that the ISS of the cured epoxy composites increases by 11.5% in comparison with the pristine CNT. Our results are also found to be generally comparable with those reported in the literature despite different matrix materials and simulation techniques (Fig. 3.33). However, most of them only paid attention to cured epoxies or thermoplastics (PE) with no crosslinked structures. For example, Sharma et al. (2015) examined the effect of functionalization using ethylene-di-amine (E-NH$_2$) functional group on the interfacial bonding characteristics of CNT-epoxy composite. They found that the amine functionalized SWCNT increases the ISS twice the pristine SWCNT. Xiao et al. (2015) studied the effects of different functionalization schemes on the interfacial strength of SWCNT-PE systems. They also found that the respective ISS is improved by 8.89%,

**Fig. 3.33** Variations in interfacial binding energy between functionalized CNTs and cured epoxy matrix with pull-out distance
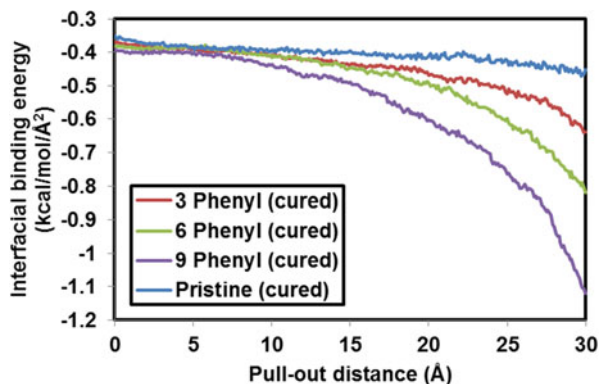
12.22%, and 31.11% for three types of alkyl groups ($C_5H_{11}/C_{10}H_{21}/C_{15}H_{31}$). Zheng et al. (2008) studied the influence of chemical functionalization on the interfacial bonding characteristics of SWCNT-reinforced polymer composites using MM and MD simulations. The simulations showed that phenyl functional group occupying only 5% of the nanotube carbon atoms drastically increases the ISS by about 1000%. Zheng et al. (2009) also used pull-out simulations to investigate the interfacial bonding characteristics between SWCNTs, on which –COOH, $-CONH_2$, $-C_6H_{11}$, or $-C_6H_5$ groups were chemically attached, and the PE matrix. They found that the ISS for $-C_6H_{11}$ and $-C_6H_5$ functionalized groups increases 3 times and 17 times compared with the pristine SWCNT, whereas the ISS for –COOH and $-CONH_2$ functionalized groups has an almost identical value to that of the pristine SWCNT. Chen et al. (2008) performed MD simulations to study the effect of chemical functionalization on the wrapping ability of the polyphenylacetylene (PPA) polymer chains. They concluded that the SWCNTs modified by methyl or phenyl groups can be well-wrapped by PPA, while the SWCNTs modified by other types of groups such as hydroxyl or –F cannot. The results also indicated that the interaction energy between the SWCNTs and PPA increases with the increase in the concentration of functionalized groups.

Unlike conventional fiber-reinforced polymer composites, CNTs offer large areas for load transfer. However, due to their unique electrical and structural properties, CNTs tend to agglomerate and aggregate and does not bond strongly with their host matrix. Therefore, the potential increase in mechanical properties of CNT-reinforced composites is limited by the degree of interfacial stress transfer. We can see from the above-mentioned results that surface modification of CNTs enhances the nanotube-matrix interfacial bonding. Besides, the modifications can also improve the CNTs' solubility and dispersibility in their nanocomposites by acting as shells to separate CNTs. Many researchers (Park and Bandaru 2010; Zou et al. 2008; Zhu et al. 2004; Tseng et al. 2007; Sun et al. 2008; Chen et al. 2006; Bekyarova et al. 2007) have investigated the effects of CNT functionalization on the mechanical properties of nanocomposites. They found that functionalized CNTs enhance the elastic modulus and tensile strength of nanocomposites, while other structural characteristics such as toughness decrease.

Fig. 3.34 Cross section of the pull-out process for 9 phenyl group functionalized CNT in cured epoxy matrix at z = 30 Å
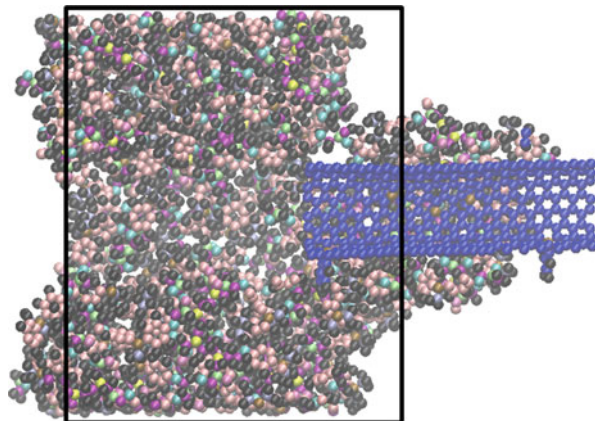
The interfacial binding energies of the functionalized CNTs for the cured epoxy systems (depicted in Fig. 3.41) are initially larger and present more prominent energy changes than that of the pristine CNTs as the pull-out process progresses. Similar to the SW defect, the initial larger interfacial binding energy is attributed to the stronger adsorption effect of the functionalized CNTs. Furthermore, the presence of a greater number of phenyl groups introduces additional molecular interactions, leading to a dramatic increase in the interfacial binding energy. It may be observed from Fig. 3.34 that a significant portion of the epoxy molecules are pulled out with the CNT during the pull-out process, indicating a stronger adhesion of the functionalized CNT with the epoxy matrix.

3.4.2   Analysis of Compressive Load Simulation

3.4.2.1   Effect of Vacancy Defect upon Freestanding SWCNTs

This section focuses on exploring the effect of different vacancy defects on the buckling behavior of freestanding SWCNTs. Based on the foregoing definitions of Sect. 3.3.2.2, buckling strain and buckling load of the pristine SWCNTs are obtained in Table 3.4. We can see that the armchair SWCNT (7, 7) possesses very similar buckling capacity compared to the zigzag SWCNT (12, 0) with the same length and diameter. However, the buckling strain of the armchair SWCNT (9, 9) is smaller than that of the armchair SWCNT (7, 7) despite the same aspect ratio. The reverse is seen when the buckling load is considered. Our results are consistent with those reported by other researchers. For instance, Wang et al. (2014) used MD simulations to study a broad range of armchair SWCNTs based on AIREBO potential. Their results showed that the buckling strain is in the range of 0.0131–0.0734 and the buckling load varies from 18.6 to 86.8 nN. Zhang et al. (2009c)

Table 3.4 Comparison of buckling behavior of freestanding defective SWCNTs against the buckling behavior of freestanding pristine SWCNTs

CNT type	CNT configuration	Buckling strain	% reduction w.r.t. pristine CNT	Buckling load (Kcal/mol-Å)	% reduction w.r.t. pristine CNT
(7, 7)	0A	0.095		1276 (89 nN)	
	1A	0.091	4.3	1208	5.3
	1B	0.084	11.3	1178	7.7
	1C	0.090	5.0	1140	10.7
	2B	0.094	0.7	1134	11.1
	2C	0.090	5.8	1215	4.8
	3A	0.092	3.0	1094	14.2
	3B	0.085	10.2	1145	10.2
	1SW-A	0.093	2.5	1130	11.5
	1SW-B	0.092	3.5	1224	4.0
(9, 9)	0A	0.091		1560 (108 nN)	
	1A	0.086	4.7	1520	2.6
	1B	0.086	5.4	1575	–0.9
	1C	0.087	4.3	1566	–0.3
	2B	0.089	1.6	1513	3.0
	2C	0.087	3.7	1543	1.1
	3A	0.087	4.2	1418	9.1
	3B	0.086	4.8	1556	0.3
	1SW-A	0.085	6.3	1489	4.6
	1SW-B	0.089	1.4	1506	3.5
(12, 0)	0A	0.094		1222 (85 nN)	
	1A	0.090	4.6	1199	1.8
	1B	0.083	11.7	1148	6.0
	1C	0.087	7.3	1104	9.7
	2B	0.090	4.3	1163	4.8
	2C	0.091	3.6	1174	3.9
	3A	0.093	0.8	1122	8.2
	3B	0.085	9.7	1117	8.6
	1SW-A	0.097	–3.1	1021	16.4
	1SW-B	0.091	3.3	1138	6.8

and Wang et al. (2010) also found that the nonlocal cylindrical shell model predicts comparable results compared with MD simulation results for SWCNTs with short aspect ratios (L/d < 8). The buckling strain can reach up to 0.1 when the aspect ratio is close to 5. Zhang et al. (2006b) investigated the effect of chirality on the buckling behavior of SWCNTs. They reported that the influence of chirality can be neglected for SWCNTs with relatively larger chiral angles.

Next, we turn our attention to the effect of vacancy defects on the buckling behavior of freestanding CNTs. Fig. 3.35 shows the strain energy-strain and the
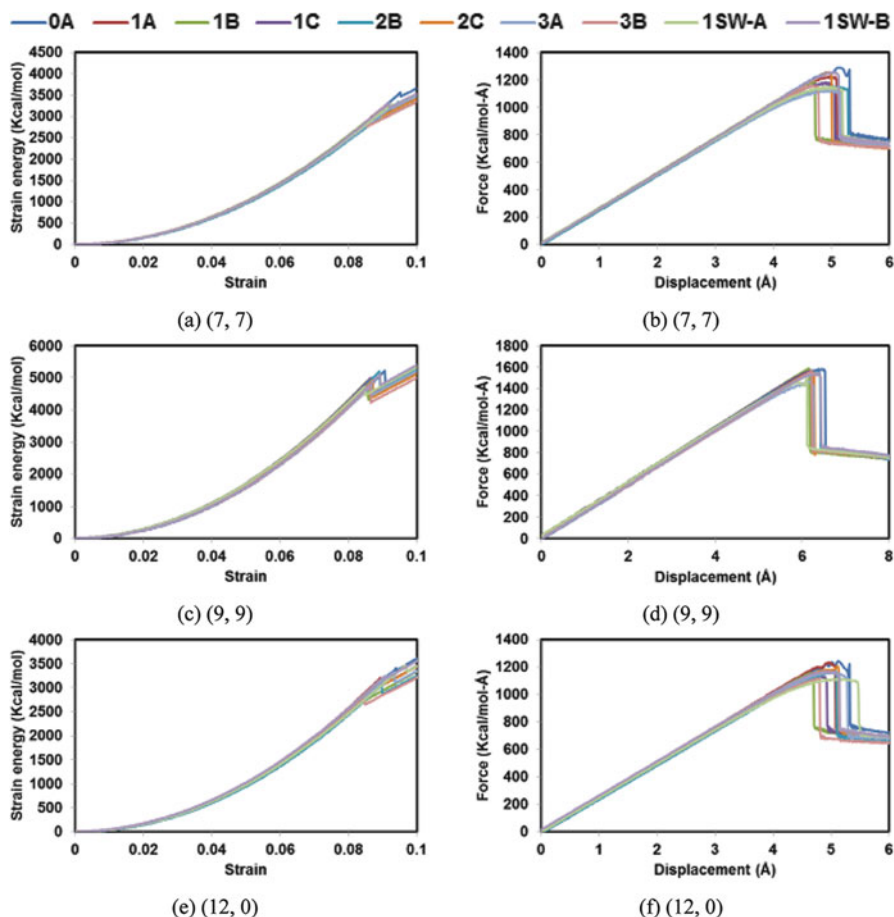
Fig. 3.35 (**a**, **c**, **e**) Strain energy-strain curves; (**b**, **d**, **f**) force-displacement curves for different freestanding defective SWCNTs

force-displacement curves for the armchairs (7, 7), (9, 9) and zigzag (12, 0) defective SWCNTs. The buckling strain and buckling load obtained based on Fig. 3.35 are compared with the pristine SWCNTs and are tabulated in Table 3.4. The buckling modes of different defective SWCNTs are depicted in Fig. 3.14. It is interesting to observe that the buckling modes of various defective SWCNTs are similar to that of the pristine SWCNTs where one flattening is formed at the mid-length. In order to study the effect of missing atoms, only the symmetric vacancies (1A), (2B), and (3A) are analyzed here. It can also be seen from the results that the monovacancy (1A) has the lowest buckling strain, but increasing the number of missing atoms decreases the buckling load irrespective of the chirality of SWCNTs. It is easy to understand that monovacancy is superior to bivacancy and trivacancy because the defective area induced by the monovacancy is obviously smaller.

However, by taking a closer look at the buckling shapes in Fig. 3.14, monovacancy tends to develop a flattening kink close to the defect, leading to excessive stress concentration. This makes the local buckling occur easily at the defect position.

The vacancies (2B), (2C), (3A), and (3B) are considered next to study the effect of symmetric and asymmetric configurations on the buckling behavior. The results for armchair SWCNTs in Table 3.4 indicate that asymmetric vacancies, compared with symmetric vacancies, cause a higher reduction in the buckling strain but not in the buckling load. This can be explained by Fig. 3.14 that asymmetric vacancies develop flattening kinks near the defect, which expedites the occurrence of the buckling. Those kinks serve to withstand more loads and increase the buckling load accordingly. However, a difference can be observed between armchair and zigzag SWCNTs. For zigzag SWCNTs, asymmetric vacancies reduce both the buckling strain and buckling load, and the buckling behavior is most affected by trivacancies. This may be due to the special bond structure of zigzag CNTs. The third focus here is on the effect of vacancy distribution on the buckling behavior of CNTs. Hence, we studied the nanotubes with vacancies (1B) and (1C). The results in Table 3.4 indicate that the vacancy (1B) has lower buckling strain but higher buckling load than the vacancy (1C). As shown in Fig. 3.14, this again occurs as a result of the positions of kinks relative to the defects. Since the monovacancies in (1B) locate exactly opposite to each other, the kinks tend to develop near the defects, leading to excessive stress concentration. This makes the vacancy (1B) easier to buckle than the vacancy (1C) but allows the vacancy (1B) to withstand higher loads for both armchair and zigzag SWCNTs.

3.4.2.2   Effect of Missing Atoms upon Embedded SWCNTs

In this section, we examine the effect of missing atoms on the buckling behavior of SWCNTs embedded in the epoxy matrix. Embedded pristine SWCNTs are initially taken as a reference to compare with freestanding pristine SWCNTs. Figure 3.13a, b shows the strain energy-strain and the force-displacement curves for the embedded pristine SWCNTs in comparison with pristine stand-alone SWCNTs. Table 3.5 shows the buckling strain and buckling load obtained from Fig. 3.13. Interestingly, the surrounding epoxy matrix significantly reduces resistance to buckling of SWCNTs by up to 43%. The reason for the embedded CNTs to have lower resistance to buckling than their freestanding counterparts is the uneven atomic forces exerted by the surrounding matrix atoms. These atomic forces deform the CNTs unevenly, leading to easier occurrence of buckling. The buckled shapes in Fig. 3.36 show that the embedded pristine CNT displays only pure shell-like buckling modes, where two flattenings referred to as "fins" by Yakobson et al. (1996) that are perpendicular to each other are formed. This is because the atomic forces exerted by the surrounding matrix atoms provide some form of confinement, preventing the CNTs from buckling sideway. The buckling shape transformation may also lead to the reduction in the buckling behavior.

Table 3.5 Comparison of buckling behavior of embedded defective SWCNTs against the buckling behavior of embedded pristine SWCNTs

Embedded CNT type	CNT configuration	Buckling strain	% reduction w.r.t. pristine CNT	Buckling load (Kcal/mol-Å)	% reduction w.r.t. pristine CNT
(7, 7)	0A	0.071		979 (68 nN)	
	1A	0.051	28.9	710	27.5
	1B	0.050	30.0	676	30.9
	1C	0.053	25.0	629	35.7
	2B	0.054	24.4	712	27.3
	2C	0.047	34.5	629	35.7
	3A	0.057	20.1	756	22.7
	3B	0.043	40.2	576	41.2
	1SW-A	0.059	17.0	784	19.9
	1SW-B	0.052	27.4	690	29.6
(9, 9)	0A	0.052		912 (63 nN)	
	1A	0.043	18.4	733	19.6
	1B	0.042	19.4	733	19.6
	1C	0.049	7.3	768	15.8
	2B	0.044	15.9	771	15.4
	2C	0.045	15.1	762	16.4
	3A	0.044	15.5	631	30.8
	3B	0.043	17.9	722	20.8
	1SW-A	0.048	7.6	866	5.1
	1SW-B	0.042	19.5	749	17.9
(12, 0)	0A	0.070		959 (67 nN)	
	1A	0.053	24.9	711	25.9
	1B	0.042	39.7	564	41.2
	1C	0.053	24.1	680	29.1
	2B	0.052	25.9	678	29.3
	2C	0.049	30.6	614	36.0
	3A	0.052	26.2	656	31.6
	3B	0.046	35.1	605	36.9
	1SW-A	0.056	20.7	750	21.8
	1SW-B	0.051	26.9	699	27.2

We now proceed to study the buckling of nanotubes with different missing atoms (1A), (2B), and (3A) embedded in the epoxy matrix. Figure 3.37 shows the strain energy-strain and the load-displacement plots for the defective embedded nanotubes discussed above. As demonstrated in Table 3.5, both the buckling strain and buckling load increase as the number of missing atoms increases. The maximum reductions in the buckling strain and buckling load are 29% and 31%, respectively, which is also higher than what we observed in freestanding defective armchair SWCNTs. This may be explained by the buckled shapes depicted in Fig. 3.36; the
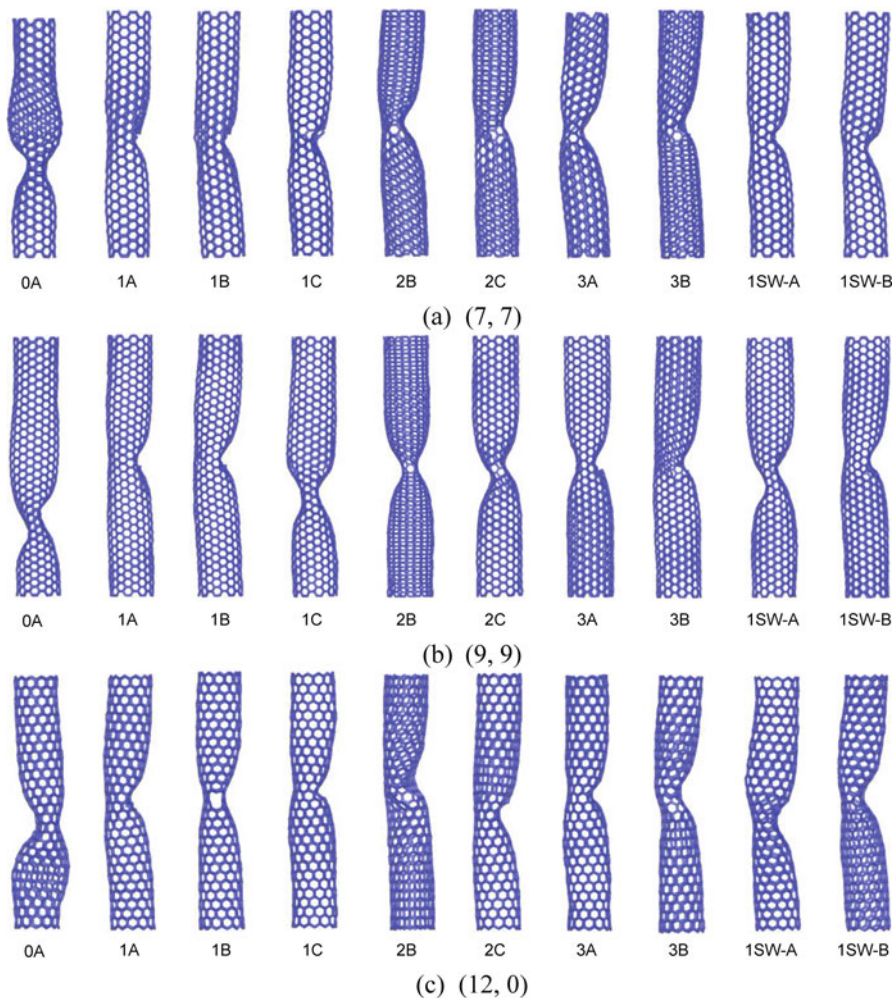
Fig. 3.36 Buckling mode shapes of the embedded SWCNTs (**a**), (7, 7), (**b**) (9, 9) and (**c**) (12, 0)

first buckling mode occurs only on one side of the SWCNTs near the missing atoms, which are neither beam-like nor shell-like buckling modes. These buckled modes depicted in Fig. 3.36 result in excessive stress concentration for monovacancies, leading to a minima of both the buckling strain and the buckling load. However, an exception can be observed for the (9, 9) SWCNT with the trivacancy (3A) which has the lowest buckling load. A closer look at the buckled shape of (3A) reveals that it displays the shell-like buckling mode due to its longer nanotube. This may contribute to a reduction in the buckling load. In contrast to the embedded defective armchair SWCNTs, Table 3.5 shows that both the buckling strain and buckling load for the embedded defective zigzag SWCNTs decrease with an increasing number of
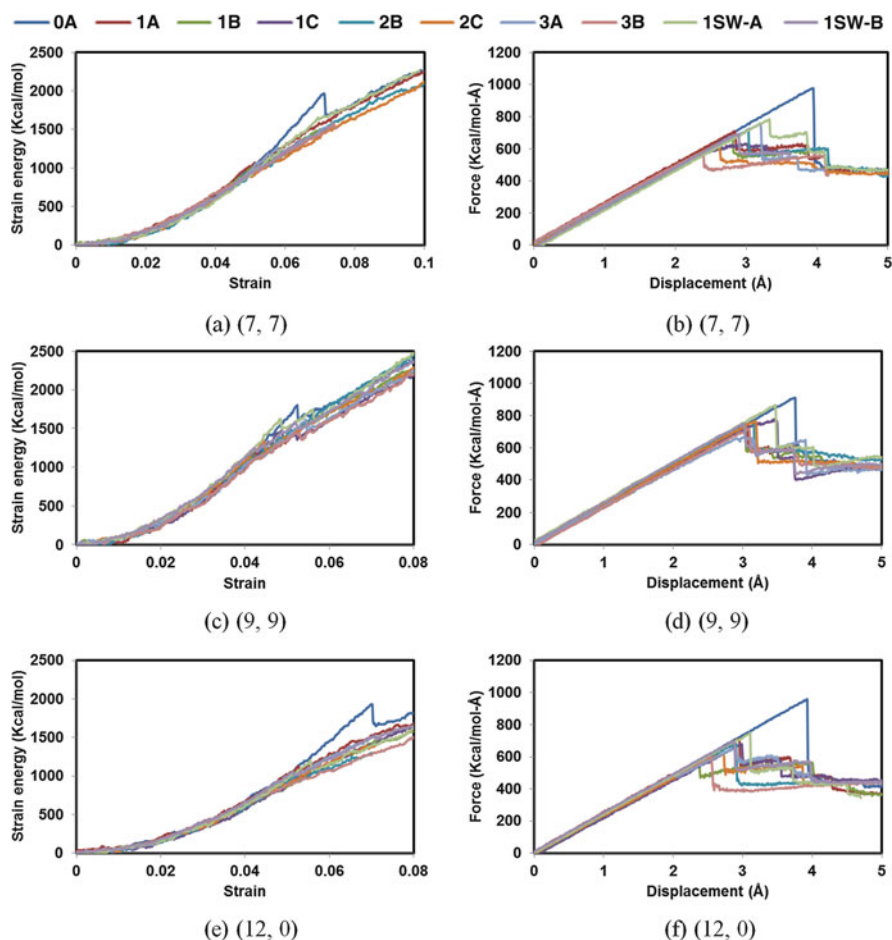
Fig. 3.37 (**a**, **c**, **e**) Strain energy-strain curves; (**b**, **d**, **f**) force-displacement curves for different embedded defective SWCNTs

missing atoms. This reveals that more missing atoms in zigzag SWCNTs have more negative influence on the buckling behavior despite similar buckling shapes to the embedded defective armchair SWCNTs.

3.4.2.3   Effect of Vacancy Symmetry and Distribution upon Embedded SWCNTs

First, let us focus on the effect of symmetric and asymmetric vacancy configurations (2B), (2C), (3A), and (3B) on the buckling behavior of embedded SWCNTs. It can be seen in Table 3.5 that asymmetric vacancies generally reduce the buckling

behavior of both armchair and zigzag SWCNTs when compared with symmetric vacancies. This is different from corresponding freestanding armchair nanotubes, where the buckling load is increased due to the presence of kinks in asymmetric vacancies. Compared with the symmetric vacancies, asymmetric vacancies further reduce the buckling strain and buckling load by 5–20%. The reason for the discrepancies may be because embedded defective SWCNTs display different buckling modes in Fig. 3.36, where the nanotubes only narrow at one side while keeping their cylindrical shapes at the other side. The position of the narrowing is close to the vacancies. However, due to the longer length in (9, 9) nanotubes, the buckling behavior of the bivacancies (2B) and (2C) is very similar to each other. They tend to buckle in a shell-like way similar to the embedded pristine SWCNTs.

Second, let us devote our attention to the effect of vacancy distribution (1B) and (1C) on the buckling behavior of embedded SWCNTs. Unlike the case of freestanding SWCNTs, both the buckling strain and buckling load of the SWCNTs containing the vacancy (1C) (see Table 3.5) are increased when compared with those of the SWCNTs containing the vacancy (1B) irrespective of the chirality of SWCNTs. This may be due to the different buckling modes presented in Fig. 3.36, which are similar to the previously investigated embedded SWCNTs. It is worth noting that there exists an anomaly for the buckling load of the (7, 7) SWCNT with the vacancy (1C). It is clear from Fig. 3.37b that the (7, 7) SWCNT with the vacancy (1C) does not show an abrupt drop in the load-displacement curve. We can see that the vacancy in the (7, 7) SWCNT helps to delay the occurrence of buckling, which increases the buckling strain, although the buckling load is still relatively low.

3.4.2.4   Effect of SW Defect upon Freestanding and Embedded SWCNTs

As shown in Table 3.4, the SW defects reduce the buckling capacity of SWCNTS in general. Similar to the vacancy symmetry of freestanding SWCNTs, asymmetry results in lower buckling strain but generally requires higher buckling load irrespective of the chirality of SWCNTs. It is noted in Fig. 3.14 that kinks tend to locate close to the asymmetric SW defect (1SW-B). This leads to excessive stress concentration, which expedites the occurrence of the buckling, and the kinks help to withstand more loads, increasing the buckling load.

The second part of this section studies the SW defects (1SW-A) and (1SW-B) of embedded SWCNTs. The embedded SWCNTs containing asymmetric SW defects (1SW-B) have lower buckling strain and buckling load (see Table 3.5) regardless of the chirality of SWCNTs. The maximum decreases in the buckling strain and buckling load are 22% and 30%, respectively, which are higher than the reduction found in their freestanding counterparts. The buckling modes for the embedded SW defective SWCNTs are similar to other embedded SWCNTs. Moreover, if we compare the buckling behavior of SW defective SWCNTs with vacancy defective SWCNTs in Table 3.5, it is evident that the SW defects (1SW-A) have the least effect on the buckling behavior of embedded SWCNTs. By contrast, the degradation effect of embedded SW defective SWCNTs (1SW-B) is very similar to the corresponding embedded vacancy defective SWCNTs.

3.5   Conclusions

In the first part of the chapter, we provided a detailed account of the effect of intrinsic defects and functionalization in CNTs upon the interfacial properties of CNT-reinforced composites. Different modeling and calculation techniques pertinent to CNT pull-out tests are presented, and proper selection of the simulation parameters are discussed. The main conclusions of the pull-out studies are summarized as follows:

(1) Deformation energy of defective CNT-reinforced polymers needs to be taken into account to obtain accurate ISS of uncured epoxy polymers.
(2) Among all the defects and functionalization, the influence of vacancy defects on the ISS was found to be significant. Moreover, the influence of the same number of missing atoms on the ISS was found to be almost identical.
(3) Adatom defects have only marginal effect on the ISS. The ISS increased for the cured epoxy systems as the number of SW defects increases.
(4) In the case of phenyl groups, the ISS of the cured systems increases due to the additional vdW interactions generated as a result of functionalization.
(5) Uncured epoxy systems have lower ISS than cured ones, and defects and functionalization do not affect the ISS very much.

The second part of this chapter is to conduct a quantitative analysis of the degradation of buckling behavior due to various types of defects (vacancy and SW defect) using MD simulations. Both freestanding and embedded SWCNTs with different size and chirality ((7, 7), (9, 9), and (12, 0)) were simulated and the results were compared with each other to understand the effect of epoxy matrix atoms. To understand the factors affecting the degree of degradation of buckling behavior, we investigated several defect configurations including the number of missing atoms, symmetry, and vacancy distribution. The main conclusions of the compressive load studies are summarized as follows:

(1) Defects generally either increase or decrease the buckling strain of freestanding and embedded SWCNTs at the same time. However, compared with those of freestanding SWCNTs, the buckling strain and buckling load for embedded SWCNTs are reduced when SWCNTs are confined in an epoxy matrix.
(2) Increasing number of missing atoms generally reduces the buckling load of freestanding SWCNTs; however, a higher number of missing atoms increases the buckling load of embedded armchair SWCNTs because the compressive force is partly supported by the kinks developed during buckling.
(3) The buckling load of freestanding SWCNTs is increased by asymmetric vacancy and SW defects, but the same defects decrease the buckling load of embedded SWCNTs due to different buckling modes.
(4) Freestanding SWCNTs containing asymmetric vacancy distribution have lower buckling load because of the positions of kinks relative to the defects, but the opposite is true for embedded SWCNTs in general.

    To sum up our findings, the defective and functionalized CNTs in cured epoxy systems can lead to increased ISS and improved load transferability. However, the presence of defects in the CNTs would ultimately result in a decrease in the effective elastic properties of the nanocomposites. A trade-off between the degradation in the mechanical properties of the defective CNTs and the improvement in the ISS of the resulting multifunctional nanocomposite systems should be carefully considered and addressed. Also, different buckling behaviors are seen between freestanding and embedded CNTs in the presence of various defects. We cannot rely on defect studies focusing only on the buckling of freestanding CNTs when designing CNT-reinforced nanocomposites. It is hoped that the findings in this chapter could contribute to deciding the expected strength from a certain sample of CNT-reinforced nanocomposites, if the degradation of buckling strain and buckling load due to different defects is known. Therefore, this chapter is also believed to be helpful in designing multifunctional nanocomposites.

References

Ajayan, P., Stephan, O., Colliex, C., Trauth, D.: Aligned carbon nanotube arrays formed by cutting a polymer resin—nanotube composite. Science. **265**, 1212–1212 (1994)

Alian, A., Kundalwal, S., Meguid, S.: Compos. Struct. **131**, 545–555 (2015a)

Alian, A., Kundalwal, S., Meguid, S.: Polymer. **70**, 149–160 (2015b)

Al-Ostaz, A., Pal, G., Mantena, P.R., Cheng, A.: J. Mater. Sci. **43**, 164–173 (2008)

Barber, A.H., Cohen, S.R., Wagner, H.D.: Appl. Phys. Lett. **82**, 4140–4142 (2003)

Barber, A.H., Cohen, S.R., Kenig, S., Wagner, H.D.: Compos. Sci. Technol. **64**, 2283–2289 (2004)

Barber, A.H., Cohen, S.R., Eitan, A., Schadler, L.S., Wagner, H.D.: Adv. Mater. **18**, 83–87 (2006)

Bekyarova, E., Thostenson, E.T., Yu, A., Itkis, M.E., Fakhrutdinov, D., Chou, T.-W., Haddon, R.C.: J. Phys. Chem. C. **111**, 17865–17871 (2007)

Bohlén, M., Bolton, K.: Comput. Mater. Sci. **68**, 73–80 (2013)

Brenner, D.W., Shenderova, O.A., Harrison, J.A., Stuart, S.J., Ni, B., Sinnott, S.B.: J. Phys. Condens. Matter. **14**, 783 (2002)

Chandra, N., Namilae, S.: Mech. Adv. Mater. Struct. **13**, 115–127 (2006)

Charlier, J.-C.: Acc. Chem. Res. **35**, 1063–1069 (2002)

Chen, W., Auad, M.L., Williams, R.J.J., Nutt, S.R.: Eur. Polym. J. **42**, 2765–2772 (2006)

Chen, H., Xue, Q., Zheng, Q., Xie, J., Yan, K.: J. Phys. Chem. C. **112**, 16514–16520 (2008)

Chen, X., Zheng, M., Park, C., Ke, C.: Small. **9**, 3345–3351 (2013)

Chen, X., Zhang, L., Zheng, M., Park, C., Wang, X., Ke, C.: Carbon. **82**, 214–228 (2015)

Cheng, Q., Wang, X.X., Ni, N.G.: Molecular dynamics simulation for compressive mechanics properties of SWCNT with random distributed vacancies. In: Bai, C., Xie, S., Zhu, X. (eds.) Nanoscience and Technology, Pts 1 and 2, pp. 1161–1164 (2007)

Chowdhury, S.C., Okabe, T.: Compos. Part A Appl. Sci. Manufacturing. **38**, 747–754 (2007)

Chowdhury, S.C., Okabe, T., Nishikawa, M.: J. Nanosci. Nanotechnol. **10**, 739–745 (2010)

Chua, P.S., Piggott, M.R.: Compos. Sci. Technol. **22**, 33–42 (1985)

Collins, P.G.: Oxford Handbook of Nanoscience and Technology: Frontiers and Advances (2010)

Cooper, C.A., Cohen, S.R., Barber, A.H., Wagner, H.D.: Appl. Phys. Lett. **81**, 3873–3875 (2002)

Cox, H.L.: British J. Appl. Phys. **3**, 72 (1952)

Dai, H., Hafner, J.H., Rinzler, A.G., Colbert, D.T., Smalley, R.E.: Nature. **384**, 147–150 (1996)

Dauber-Osguthorpe, P., Roberts, V.A., Osguthorpe, D.J., Wolff, J., Genest, M., Hagler, A.T.: Proteins Structure Function Bioinformatics. **4**, 31–47 (1988)

Desai, A.V., Haque, M.A.: Thin-Walled Struct. **43**, 1787–1803 (2005)

Frankland, S., Caglar, A., Brenner, D., Griebel, M.: J. Phys. Chem. B. **106**, 3046–3048 (2002)

Ganesan, Y., Peng, C., Lu, Y., Loya, P.E., Moloney, P., Barrera, E., Yakobson, B.I., Tour, J.M., Ballarini, R., Lou, J.: ACS Appl. Mater. Interfaces. **3**, 129–134 (2011)

Ganesan, Y., Salahshoor, H., Peng, C., Khabashesku, V., Zhang, J., Cate, A., Rahbar, N., Lou, J.: J. Appl. Phys. **115**, 224305 (2014)

Gao, X.L., Li, K.: Int. J. Solids Struct. **42**, 1649–1667 (2005)

Gou, J.H., Minaie, B., Wang, B., Liang, Z.Y., Zhang, C.: Comput. Mater. Sci. **31**, 225–236 (2004)

Gou, J., Liang, Z., Zhang, C., Wang, B.: Compos. Part B Eng. **36**, 524–533 (2005)

Hao, X., Qiang, H., Yao, X.: Compos. Sci. Technol. **68**, 1809–1814 (2008)

Hashimoto, A., Suenaga, K., Gloter, A., Urita, K., Iijima, S.: Nature. **430**, 870–873 (2004)

Humphrey, W., Dalke, A., Schulten, K.: J. Mol. Graph. **14**, 33–38 (1996)

Iijima, S.: Nature. **354**, 56–58 (1991)

Iijima, S., Brabec, C., Maiti, A., Bernholc, J.: J. Chem. Phys. **104**, 2089–2092 (1996)

Jang, C., Lacy, T.E., Gwaltney, S.R., Toghiani, H., Pittman Jr., C.U.: Polymer. **54**, 3282–3289 (2013)

Joshi, U.A., Sharma, S.C., Harsha, S.P.: Comput. Mater. Sci. **50**, 3245–3256 (2011)

Kitipornchai, S., He, X., Liew, K.: J. Appl. Phys. **97**, (2005)

Kulathunga, D.D.T.K., Ang, K.K.: Comput. Mater. Sci. **81**, 233–238 (2014)

Kulathunga, D.D.T.K., Ang, K.K., Reddy, J.N.: J. Phys. Condens. Matter. **22**, (2010)

Kumar, A., Sundararaghavan, V., Browning, A.R.: Modell. Simulation Mater. Sci. Eng. **22**, 025013 (2014)

Lau, K.-T.: Chem. Phys. Lett. **370**, 399–405 (2003)

Lenosky, T., Gonze, X., Teter, M., Elser, V.: Energetics of negatively curved graphitic carbon. Nature. **355**, 333–335 (1992)

Li, C., Chou, T.-W.: J. Nanosci. Nanotechnol. **3**, 423–430 (2003a)

Li, C., Chou, T.-W.: Int. J. Solids Struct. **40**, 2487–2499 (2003b)

Li, K., Saigal, S.: Mater. Sci. Eng. A. **457**, 44–57 (2007)

Li, Y., Liu, Y., Peng, X., Yan, C., Liu, S., Hu, N.: Comput. Mater. Sci. **50**, 1854–1860 (2011)

Li, C., Medvedev, G.A., Lee, E.-W., Kim, J., Caruthers, J.M., Strachan, A.: Polymer. **53**, 4222–4230 (2012)

Liao, K., Li, S.: Appl. Phys. Lett. **79**, 4225–4227 (2001)

Liew, K.M., He, X.Q., Kitipornchai, S.: Proc. R. Soc. Math. Phys. Eng. Sci. **461**, 3785–3805 (2005)

Liu, L., Barber, A.H., Nuriel, S., Wagner, H.D.: Adv. Funct. Mater. **15**, 975–980 (2005)

Liu, J.Q., Xiao, T., Liao, K., Wu, P.: Nanotechnology. **18**, 165701 (2007)

Lourie, O., Wagner, H.D.: Appl. Phys. Lett. **73**, 3527–3529 (1998)

Lourie, O., Wagner, H.: Compos. Sci. Technol. **59**, 975–977 (1999)

Lourie, O., Cox, D., Wagner, H.: Phys. Rev. Lett. **81**, 1638 (1998)

Mahboob, M., Islam, M.Z.: Comput. Mater. Sci. **79**, 223–229 (2013)

Martínez, L., Andrade, R., Birgin, E.G., Martínez, J.M.: J. Comput. Chem. **30**, 2157–2164 (2009)

Meguid, S.A., Sun, Y.: Mater. Des. **25**, 289–296 (2004)

Meguid, S.A., Wernik, J.M., Cheng, Z.Q.: Int. J. Solids Struct. **47**, 1723–1736 (2010)

Meyer, J.C., Kisielowski, C., Erni, R., Rossell, M.D., Crommie, M., Zettl, A.: Nano Lett. **8**, 3582–3586 (2008)

Motevalli, B., Montazeri, A., Liu, J.Z., Rafii-Tabar, H.: Comput. Mater. Sci. **79**, 619–626 (2013)

Namilae, S., Chandra, N.: Compos. Sci. Technol. **66**, 2030–2038 (2006)

Nardelli, M.B., Yakobson, B.I., Bernholc, J.: Phys. Rev. Lett. **81**, 4656 (1998)

Natsuki, T., Wang, F., Ni, Q.Q., Endo, M.: J. Mater. Sci. **42**, 4191–4196 (2007)

Newcomb, B.A., Chae, H.G., Gulgunje, P.V., Gupta, K., Liu, Y., Tsentalovich, D.E., Pasquali, M., Kumar, S.: Polymer. **55**, 2734–2743 (2014)

Pan, Z.W., Xie, S.S., Lu, L., Chang, B.H., Sun, L.F., Zhou, W.Y., Wang, G., Zhang, D.L.: Appl. Phys. Lett. **74**, 3152–3154 (1999)

Park, S.H., Bandaru, P.R.: Polymer. **51**, 5071–5077 (2010)

Parvaneh, V., Shariati, M., Sabed, A.M.M.: Eur. J. Mech. Solids. **28**, 1072–1078 (2009)

Pavia, F., Curtin, W.A.: Acta Mater. **59**, 6700–6709 (2011)

Pavia, F., Curtin, W.A.: J. Mech. Phys. Solids. **61**, 1971–1982 (2013)

Plimpton, S.: J. Comput. Phys. **117**, 1–19 (1995)

Poelma, R.H., Sadeghian, H., Koh, S., Zhang, G.Q.: Microelectronics Reliability. **52**, 1279–1284 (2012)

Qian, D., Dickey, E.C.: J. Microsc. **204**, 39–45 (2001)

Qian, D., Dickey, E.C., Andrews, R., Rantell, T.: Appl. Phys. Lett. **76**, 2868–2870 (2000)

Quek, M.Y.: Int. J. Adhesion Adhesives. **22**, 303–310 (2002)

Ranjbartoreh, A.R., Wang, G.: Nanoscale Res. Lett. **6**, (2011)

Roy, D., Bhattacharyya, S., Rachamim, A., Plati, A., Saboungi, M.-L.: J. Appl. Phys. **107**, 043501 (2010)

Ru, C.: J. Appl. Phys. **87**, 7227–7231 (2000)

Ru, C.: J. Mech. Phys. Solids. **49**, 1265–1279 (2001)

Schadler, L., Giannaris, S., Ajayan, P.: Appl. Phys. Lett. **73**, 3842–3844 (1998)

Sharma, S., Chandra, R., Kumar, P., Kumar, N.: Comput. Mater. Sci. **86**, 1–8 (2014)

Sharma, K., Sen Kaushalyayan, K., Shukla, M.: Comput. Mater. Sci. **99**, 232–241 (2015)

Spitalsky, Z., Tasis, D., Papagelis, K., Galiotis, C.: Prog. Polym. Sci. **35**, 357–401 (2010)

Suenaga, K., Wakabayashi, H., Koshino, M., Sato, Y., Urita, K., Iijima, S.: Nat. Nanotechnol. **2**, 358–360 (2007)

Sun, H.: J. Phys. Chem. B. **102**, 7338–7364 (1998)

Sun, L., Warren, G.L., O'Reilly, J.Y., Everett, W.N., Lee, S.M., Davis, D., Lagoudas, D., Sue, H.J.: Carbon. **46**, 320–328 (2008)

Talukdar, K., Agrawala, R., Mitra, A.K.: New Carbon Mater. **26**, 408–416 (2011)

Thostenson, E.T., Li, C., Chou, T.-W.: Compos. Sci. Technol. **65**, 491–516 (2005)

Timoshenko, S.: Theory of Elastic Stability. McGraw-Hill, New York (1961)

Tseng, C.H., Wang, C.C., Chen, C.Y.: Chem. Mater. **19**, 308–315 (2007)

Tsuda, T., Ogasawara, T., Deng, F., Takeda, N.: Compos. Sci. Technol. **71**, 1295–1300 (2011)

Tu, Z.-C., Ou-Yang, Z.-C.: Phys. Rev. B. **65**, 233407 (2002)

Wagner, H.D.: Chem. Phys. Lett. **361**, 57–61 (2002)

Wagner, H., Lourie, O., Feldman, Y., Tenne, R.: Appl. Phys. Lett. **72**, 188–190 (1998)

Wang, C.Y., Ru, C.Q., Mioduchowski, A.: Int. J. Solids Struct. **40**, 3893–3911 (2003)

Wang, Q., Varadan, V.K., Xiang, Y., Han, Q.K., Wen, B.C.: Int. J. Struct. Stability Dyn. **8**, 357–366 (2008)

Wang, C., Zhang, Y., Xiang, Y., Reddy, J.: Appl. Mech. Rev. **63**, 030804 (2010)

Wang, C., Chowdhury, A.R., Koh, S., Zhang, Y.: Molecular dynamics simulation and continuum shell model for buckling analysis of carbon nanotubes. In: Modeling of Carbon Nanotubes, Graphene and their Composites, pp. 239–273. Springer International Publishing (2014)

Wei, C.Y.: Appl. Phys. Lett. **88**, (2006)

Wernik, J.M., Meguid, S.A.: Acta Mech. **212**, 167–179 (2010)

Wernik, J.M., Meguid, S.A.: Acta Mech. **217**, 1–16 (2011)

Wernik, J.M., Cornwell-Mott, B.J., Meguid, S.A.: Int. J. Solids Struct. **49**, 1852–1863 (2012)

Wong, E.W., Sheehan, P.E., Lieber, C.M.: Science. **277**, 1971–1975 (1997)

Wong, M., Paramsothy, M., Xu, X.J., Ren, Y., Li, S., Liao, K.: Polymer. **44**, 7757–7764 (2003)

Xiao, S., Hou, W.: Phys. Rev. B. **73**, 115406 (2006)

Xiao, K., Zhang, L.: J. Mater. Sci. **39**, 4481–4486 (2004)

Xiao, T., Liu, J., Xiong, H.: Acta Mech. Solida Sin. **28**, 277–284 (2015)

Xin, H., Han, Q., Yao, X.-H.: Carbon. **45**, 2486–2495 (2007)

Xiong, Q.L., Meguid, S.A.: Eur. Polymer J. (2015)

Xu, X., Thwe, M.M., Shearwood, C., Liao, K.: Appl. Phys. Lett. **81**, 2833–2835 (2002)

Yakobson, B.I., Brabec, C.J., Bernholc, J.: Phys. Rev. Lett. **76**, 2511–2514 (1996)

Yang, S., Choi, J., Cho, M.: Compos. Struct. **127**, 108–119 (2015)

Zhang, Y.C., Wang, X.: Int. J. Solids Struct. **42**, 5399–5412 (2005)

Zhang, Y.Y., Wang, C.M., Tan, V.B.C.: J. Eng. Mech. **132**, 952–958 (2006a)

Zhang, Y., Tan, V., Wang, C.: J. Appl. Phys. **100**, 074304 (2006b)

Zhang, Y.Y., Wang, C.M., Tan, V.B.C.: Nanotechnology. **20**, (2009a)

Zhang, Y.Y., Xiang, Y., Wang, C.M.: J. Appl. Phys. **106**, (2009b)

Zhang, Y., Wang, C., Duan, W., Xiang, Y., Zong, Z.: Nanotechnology. **20**, 395707 (2009c)

Zheng, Q., Xue, Q., Yan, K., Gao, X., Li, Q., Hao, L.: Polymer. **49**, 800–808 (2008)

Zheng, Q.B., Xia, D., Xue, Q.Z., Yan, K.Y., Gao, X.L., Li, Q.: Appl. Surf. Sci. **255**, 3534–3543 (2009)

Zhou, L.G., Shi, S.Q.: Carbon. **41**, 613–615 (2003)

Zhou, L.-M., Mai, Y.-W., Ye, L.: Compos. Eng. **5**, 1199–1219 (1995)

Zhu, J., Peng, H., Rodriguez-Macias, F., Margrave, J.L., Khabashesku, V.N., Imam, A.M., Lozano, K., Barrera, E.V.: Adv. Funct. Mater. **14**, 643–648 (2004)

Zou, W., Du, Z.-J., Liu, Y.-X., Yang, X., Li, H.-Q., Zhang, C.: Compos. Sci. Technol. **68**, 3259–3264 (2008)